Ore Geology Reviews 138 (2021) 104417

Contents lists available at ScienceDirect

Ore Geology Reviews

journal homepage: www.elsevier.com/locate/oregeorev

Corundum (ruby) growth during the final assembly of the Archean North Atlantic Craton, southern West Greenland

Chris Yakymchuk [a,*], Vincent van Hinsberg [b], Christopher L. Kirkland [c], Kristoffer Szilas [d], Carson Kinney [a], Jillian Kendrick [a], Julie A. Hollis [e]

[a] Department of Earth and Environmental Sciences, University of Waterloo, Waterloo, Ontario N2L 3G1, Canada
[b] GEOTOP Research Centre, Department of Earth and Planetary Sciences, McGill University, 3450 Rue University, Montréal, Québec H3A 0E8, Canada
[c] School of Earth and Planetary Science, Centre for Exploration Targeting – Curtin Node, Curtin University, Perth, Western Australia 6102, Australia
[d] Department of Geosciences and Natural Resource Management, University of Copenhagen, Øster Voldgade 10, DK-1350 Copenhagen K, Denmark
[e] Department of Geology, Ministry of Mineral Resources, Government of Greenland, P.O. Box 930, 3900 Nuuk, Greenland

ARTICLE INFO

Keywords:
Archean
Supracrustal rocks
Maniitsoq
Corundum
Ruby
Biogenic carbon
Graphite

ABSTRACT

We investigate the petrogenesis and tectonic significance of corundum (ruby)-bearing late Neoarchean rocks from the Maniitsoq region of southern West Greenland using petrology, thermobarometry, phase equilibrium modelling, and carbon isotopes as well as U–Pb zircon and rutile geochronology. Corundum was generated by amphibolite-facies metamorphism of an aluminosilicate schist. Thermobarometry and phase equilibrium modelling constrain the *P–T* conditions of corundum growth to ~ 600–700 °C at ~ 4–7 kbar. The presence of graphite suggests corundum growth in the presence of a mixed hydrous–carbonic fluid; this fluid was responsible for the transfer of SiO_2 out of the precursor rock generating quartz-undersaturated conditions that enabled corundum growth. Carbon isotope values of graphite from corundum-bearing schist indicate a biogenic origin and are inconsistent with the fractionation of non-biogenic carbon. Zircon U–Pb geochronology documents regional metamorphism at *c.* 2.72–2.60 Ga. U–Pb rutile geochronology yields an upper intercept age of *c.* 2.5 Ga, which is interpreted as the best age estimate of corundum growth. The growth of corundum in southern West Greenland reflects heating associated with post-tectonic magmatism after the assembly of the North Atlantic Craton.

1. Introduction

Gem-quality corundum (ruby and sapphire) is generated through a combination of metamorphic, metasomatic and, rarely, igneous processes that affect or generate silica-undersaturated rocks. Metamorphic ruby deposits can form during high-temperature metamorphism that accompanies anatexis (Cartwright and Barnicoat, 1986; Simonet et al., 2008) or at lower metamorphic grades associated with metasomatism (e.g. Giuliani et al., 2003; Owens et al., 2013; Zhang et al., 2018). Ruby can also form during high-temperature metamorphism after crustal thickening caused by continental collision (Stern et al., 2013); therefore, the tectonic history of a terrane can be intimately linked with its prospectivity for ruby formation. Although the protolith to ruby-bearing lithologies can vary, aluminous sedimentary rocks may provide an Al-rich precursor to grow corundum if silica is removed during their metamorphic evolution (e.g. Riesco et al., 2005; Yakymchuk and Szilas, 2018; van Hinsberg et al., 2021). However, the timing of corundum growth relative to the metamorphic cycle is commonly difficult to constrain, yet this information is crucial for understanding the thermochemical conditions required for ruby (and sapphire) growth within metamorphic systems, their relationship to regional tectonothermal events, and for developing strategies for predictive gem exploration.

The Akia Terrane in southwestern Greenland experienced a complex tectonic history with Mesoarchean crustal growth followed by extensive polyphase deformation during Neoarchean reworking with final amalgamation of the North Atlantic Craton occurring at *c.* 2.7 Ga (e.g. Nutman and Friend, 2007). Corundum deposits in the Akia Terrane are hosted by metamorphosed igneous and sedimentary rocks of various ages. The most famous corundum locality in Greenland is the Aappaluttoq ruby deposit hosted by the Mesoarchaean Fiskenæsset Anorthosite Complex (Herd et al., 1969; Keulen and Kalvig, 2013; Keulen et al., 2014; Smith et al., 2016; Keulen et al., 2020). Corundum from the

* Corresponding author.
E-mail address: chris.yakymchuk@uwaterloo.ca (C. Yakymchuk).

https://doi.org/10.1016/j.oregeorev.2021.104417
Received 15 March 2021; Received in revised form 26 July 2021; Accepted 13 August 2021
Available online 20 August 2021

Aappaluttoq deposit was recently dated at 2686 + 300/−74 Ma using offline laser ablation followed by thermal ionization mass spectrometry to obtain a Pb–Pb isochron (Krebs et al., 2019). Although this age has large uncertainties, it is probably younger than the age of the complex (*c.* 2970 Ma; Polat et al., 2010), and demonstrates that late-orogenic metamorphic and metasomatic processes were probably responsible for the formation of corundum. Keulen et al., (2020) propose that c. 2710 Ma pegmatites drove ruby formation in the Aappaluttoq deposit. Ruby mineralization at Storø (Fig. 1) was associated with metasomatism and is older than a *c.* 2.50 Ma age of rutile from the host rock, and may be associated with late Neoarchean magmatism in that region (van Hinsberg et al., 2021)

In the Maniitsoq region, corundum is hosted by metasedimentary rocks within a late-orogenic shear zone (Dyck et al., 2015) where the stability of corundum was shown to mainly be controlled by highly aluminous and silica-deficient conditions at elevated pressure and temperature (Yakymchuk and Szilas, 2018) and was probably accompanied by metasomatism (Garde and Marker, 1988). However, the

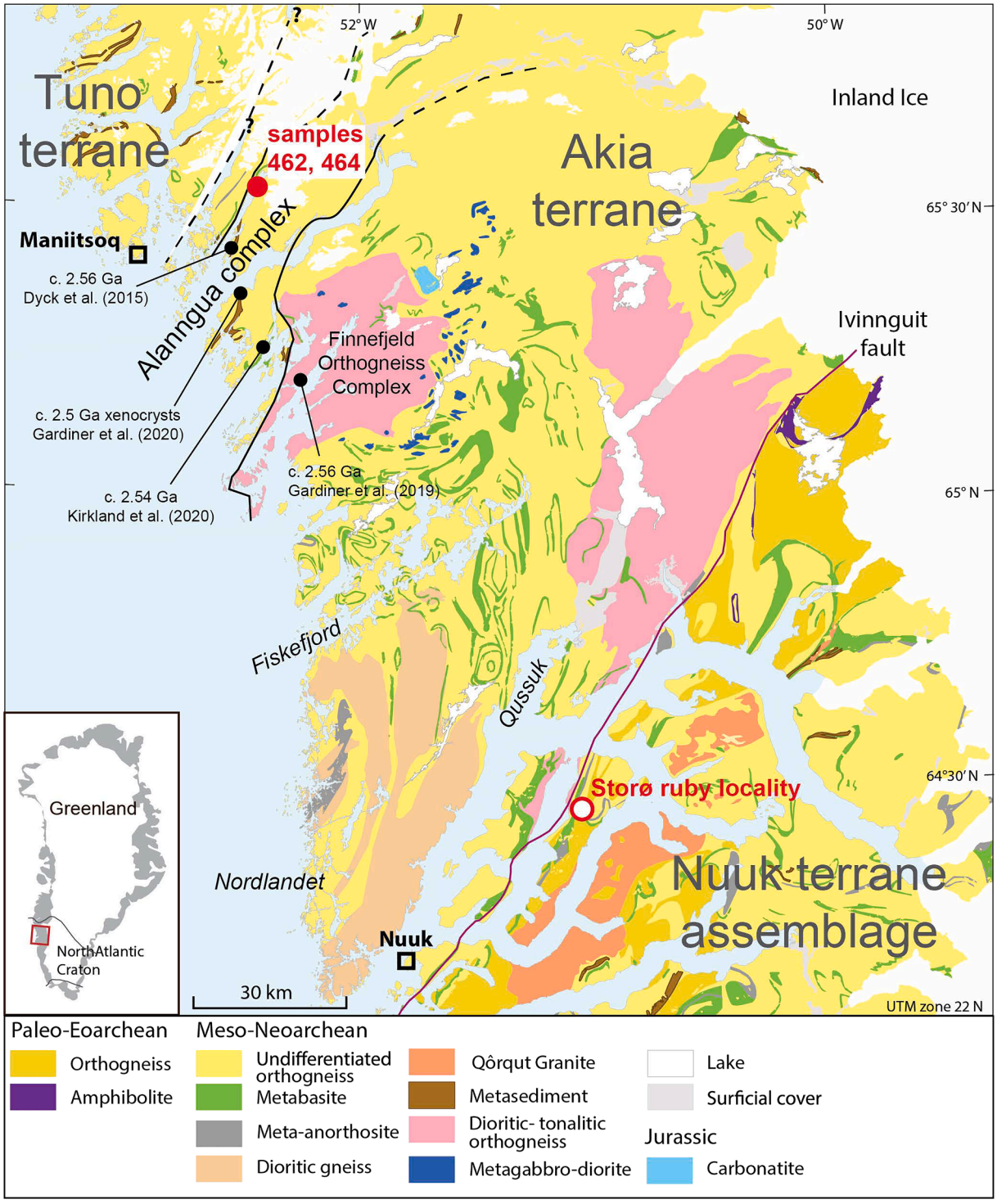

Fig. 1. Simplified geological map of the Akia Terrane in the North Atlantic Craton showing the location of the Maniitsoq ruby occurrence (samples 462, 464). Map modified from Allaart (1982) and Gardiner et al. (2019). Terrane boundaries are from Steenfelt et al. (2021). Locations of late Neoarchean zircon ages are shown.

timing of corundum formation in the Maniitsoq region relative to regional tectonothermal events is not known nor is its temporal and tectonic relationship to other corundum deposits in the Akia Terrane and the North Atlantic Craton. Yet, this information is important for developing regional-scale prospecting models for ruby genesis and understanding the petrotectonic mechanisms needed to generate ruby deposits.

In this contribution, we combine petrography, mineral thermometry, phase equilibrium modelling, and carbon isotope analysis to evaluate corundum (ruby) petrogenesis in the Maniitsoq region and elucidate the timing of metamorphism and corundum growth relative to regional tectonothermal events using zircon and rutile U–Pb geochronology. Combined with the results of a companion study (van Hinsberg et al., 2021), these new insights provide important constraints on the relative timing of ruby growth in orogenic cycles, enhance our understanding of indicators for ruby prospecting in Archean terranes, and link corundum (ruby) growth to a crucial time in the Archean Eon when the global transition to subduction-driven plate tectonics was well underway.

2. Regional geology

The North Atlantic Craton (NAC) of southern West Greenland is dominated by Archean continental crust of the tonalite-trondhjemite-granodiorite (TTG) suite ranging in age from *c.* 3.8 to 2.8 Ga (Friend and Nutman, 2001; Friend and Nutman, 2019). Although orthogneiss of TTG parentage is volumetrically dominant (Fig. 1), other important constituents include anorthosite and layered norite-peridotite complexes, which mostly predate TTG crust (Polat et al., 2010; Szilas et al., 2015; 2018; Waterton et al., 2020). Supracrustal greenstone belts composed of metavolcanic and metasedimentary rocks form disaggregated belts (Fig. 1) that are pervasively deformed and deposition postdated most TTG magmatism (Polat et al., 2011; Szilas, 2018; Kirkland et al., 2018a). Late-stage granites (*s.s.*)—such as the Qôrqut Granite Complex (Nutman et al., 2010)— at *c.* 2.56 Ga mark the end of cratonization in this region, although Proterozoic mafic dykes intruded during discrete events from 2.5 Ga to 1.8 Ga (Kalsbeek and Taylor, 1985).

The Maniitsoq region—defined here as extending from Fiskefjord in the south to Maniitsoq Island in the north—is dominated by 3.2 to 3.0 Ga TTG and dioritic gneiss (Gardiner et al., 2019), and records two granulite-facies metamorphic events at *c.* 3.0 Ga and *c.* 2.85–2.70 Ga (Kirkland et al., 2018a, Yakymchuk et al., 2020) as well as another potential event at 2.55 Ga evident in a shear zone near Maniitsoq (Dyck et al., 2015). The corundum occurrence investigated here is found at the northern margin of the Alanngua complex (Steenfelt et al., 2021) that is a cryptic boundary between the Mesoarchean Akia terrane to the southeast and the younger, mainly Neoarchean Tuno terrane to the northwest (Fig. 1). The Alanngua complex contains a larger proportion of metasedimentary rocks than the surrounding terranes and contains Neoarchean magmatic and metamorphic ages that are potentially distinct from those in the Akia and Tuno terranes (Steenfelt et al., 2021).

Corundum in the Maniitsoq region is hosted by aluminous metasedimentary rocks in tectonic contact with ultramafic enclaves (Ramberg, 1948; Garde and Marker 1988; Yakymchuk and Szilas 2018). Note that we use *corundum* here to encompass both *gem*-quality occurrences of red–pink corundum (i.e. ruby) and accompanying non-gem quality material. Corundum growth in the metasedimentary rocks was associated with the establishment of a chemical potential gradient during metamorphism that transferred silica to adjacent metaultramafic rocks via anatectic melt or fluid; chromium was also transferred to the aluminous gneiss resulting in Cr-rich corundum (Yakymchuk and Szilas, 2018). The metamorphic mineral assemblages in the corundum-bearing rocks and their inferred precursors are compatible with a wide range of pressure–temperature (*P*–*T*) conditions and were assumed by Yakymchuk and Szilas (2018) to be related to a regional *c.* 2.85–2.70 Ga high-temperature metamorphic event. Recent work has also documented fluid movement at *c.* 2.6–2.5 Ga in the Maniitsoq region (Dyck et al., 2015; Kirkland et al., 2018b, 2020) and it is unclear if corundum grew during these younger (late Neoarchean) events associated with the terminal stages of orogenesis and assembly of the North Atlantic Craton. Nonetheless, this information is important for understanding the confluence of thermochemical factors that drove ruby growth and provides keys insight for future prospecting.

3. Sample materials and petrography

Samples were collected from a corundum occurrence to the east of Maniitsoq (Fig. 1) as previously investigated by Yakymchuk and Szilas (2018) and van Hinsberg et al. (2021). The locality includes a corundum-bearing schist (~2 m wide) that is spatially between ultramafic rocks and an aluminosilicate gneiss (Fig. 2a). Corundum is located at the tectonic boundary between an aluminous gneiss and ultramafic enclaves (Fig. 2b). Corundum, which is hosted in a biotite-rich schist (Fig. 2c, d), can be macroscopically zoned in colour and often encloses macroscopic to microscopic graphite inclusions (Fig. 2e). One sample of a corundum schist (sample 464; 65.5681′N, –52.3900′W) and its inferred precursor (aluminosilicate gneiss; sample 462; 65.5688′N, –52.3876′W) are investigated in detail in this study and the petrography and microstructures are summarized below. On the opposite side of the aluminosilicate gneiss away from the corundum schist is an amphibolite that contains very minor amounts of macroscopic calcite several tens of meters away from the corundum schist; no other macroscopic carbonate minerals were identified at this locality. No leucosome was observed within or near the corundum schist, but leucosome is present in the amphibolite tens of meters away. The only macroscopic evidence of fluid–rock interaction are 10–30 cm wide amphibole-rich zones associated with fractures in the ultramafic rocks.

3.1. Maniitsoq corundum-bearing schist

Sample 464 is a heterogeneous corundum-bearing schist (Fig. 2c, d) composed of two main mineralogical domains: (1) biotite aggregates (~60 vol%) associated with large corundum crystals (~40 vol%) and, (2) fine-grained biotite (~50 vol%) + plagioclase (~45 vol%) + staurolite (~3 vol%) + corundum domains (~2 vol%) (Fig. 3a). In the biotite-rich aggregates (domain 1), biotite laths up to 2 mm in length are moderately aligned, defining the foliation of the rock, and wrap around subidioblastic corundum up to 2 cm in diameter (Fig. 3a–c). Corundum contains inclusions of biotite, graphite (Fig. 2d), staurolite, rutile, and Fe-sulphide, which may be concentrated near the rim or in discrete, inclusion-rich patches randomly within the crystal (Fig. 3c). An uncommon feature of the biotite-aggregate domain is trace amounts of pale green hornblende (Fig. 3b), which forms elongate crystals up to 0.8 mm in length.

In the finer-grained domains (domain 2; Fig. 3a), subidioblastic biotite and plagioclase are ~ 0.5 mm in size and evenly distributed. Xenoblastic staurolite (up to 2 mm) is found in plagioclase-rich patches (Fig. 3d). Corundum in this domain forms clusters of subidioblastic crystals up to 0.2 mm in size that are spatially associated with staurolite (Fig. 3d, e). Rutile is distributed throughout each domain (Fig. 3b, c, and e) and can be localized in rutile-rich clusters (Fig. 3a). Graphite is also found in both domains, typically in association with biotite, and thus is most abundant in biotite-rich domains (Fig. 3b, c, and e). Rare tourmaline (<1 vol%) is heterogeneously distributed. When present, tourmaline occurs as isolated grains in domain 2 and as large grains or clusters associated with corundum in domain 1 (van Hinsberg et al., 2021).

3.2. Maniitsoq aluminosilicate gneiss

Sample 462 is a garnet–sillimanite–kyanite gneiss (Fig. 2b) with undulating foliation defined by aligned biotite, sillimanite, and kyanite in compositionally distinct bands (up to 3 mm thick) of sillimanite ±

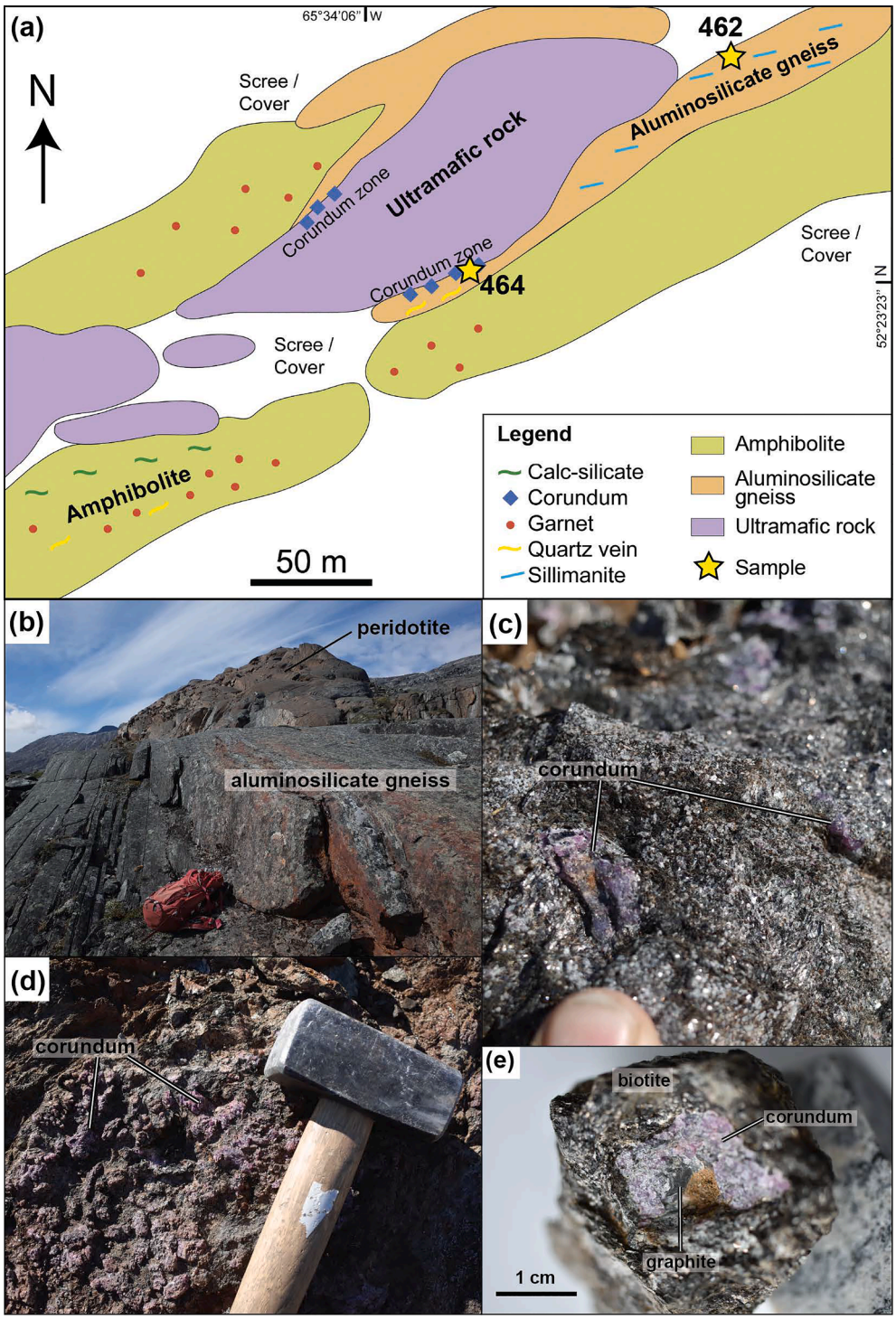

Fig. 2. Map and field photos of the Maniitsoq corundum locality. (a) Simplified geological map of the locality showing the sampling locations (modified from Yakymchuk and Szilas, 2018). (b) Layered aluminosilicate gneiss (sample 462) in the foreground and ultramafic body (peridotite) in the background (brown hill). (c) Corundum in a biotite-rich matrix (sample 464). (d) Cluster of corundum grains in mica schist (sample 464). (e) Graphite inclusion in corundum from Maniitsoq.

kyanite, quartz ± plagioclase, and biotite + quartz + plagioclase ± sillimanite (Fig. 4a, b, and c). Kyanite is locally rimmed by sillimanite (Fig. 4b) in shear bands indicating that kyanite was early. The foliation is deflected around garnet porphyroblasts (up to 1 cm and representing ~ 20 vol% of the sample) containing inclusions of quartz, rutile, ilmenite, sillimanite, biotite, rare calcite, tourmaline and staurolite (Fig. 4a, d). Some biotite crystals are rimmed by fine-grained sillimanite (Fig. 4c). Small staurolite crystals (up to 100 μm) are uncommon within the matrix (Fig. 4d) and represent ~ 3 vol% of the sample; other accessory minerals include rutile (~1 vol%), ilmenite (~2 vol%), tourmaline (<1 vol%), and apatite (Fig. 4a, c, d). Rutile and ilmenite are present in the matrix and as inclusions in garnet. Minor graphite (≪1 vol %) is found in the matrix. Tourmaline (<1 vol%) occurs as small (<2 μm) grains in quartz-rich layers (e.g. van Hinsberg et al., 2021).

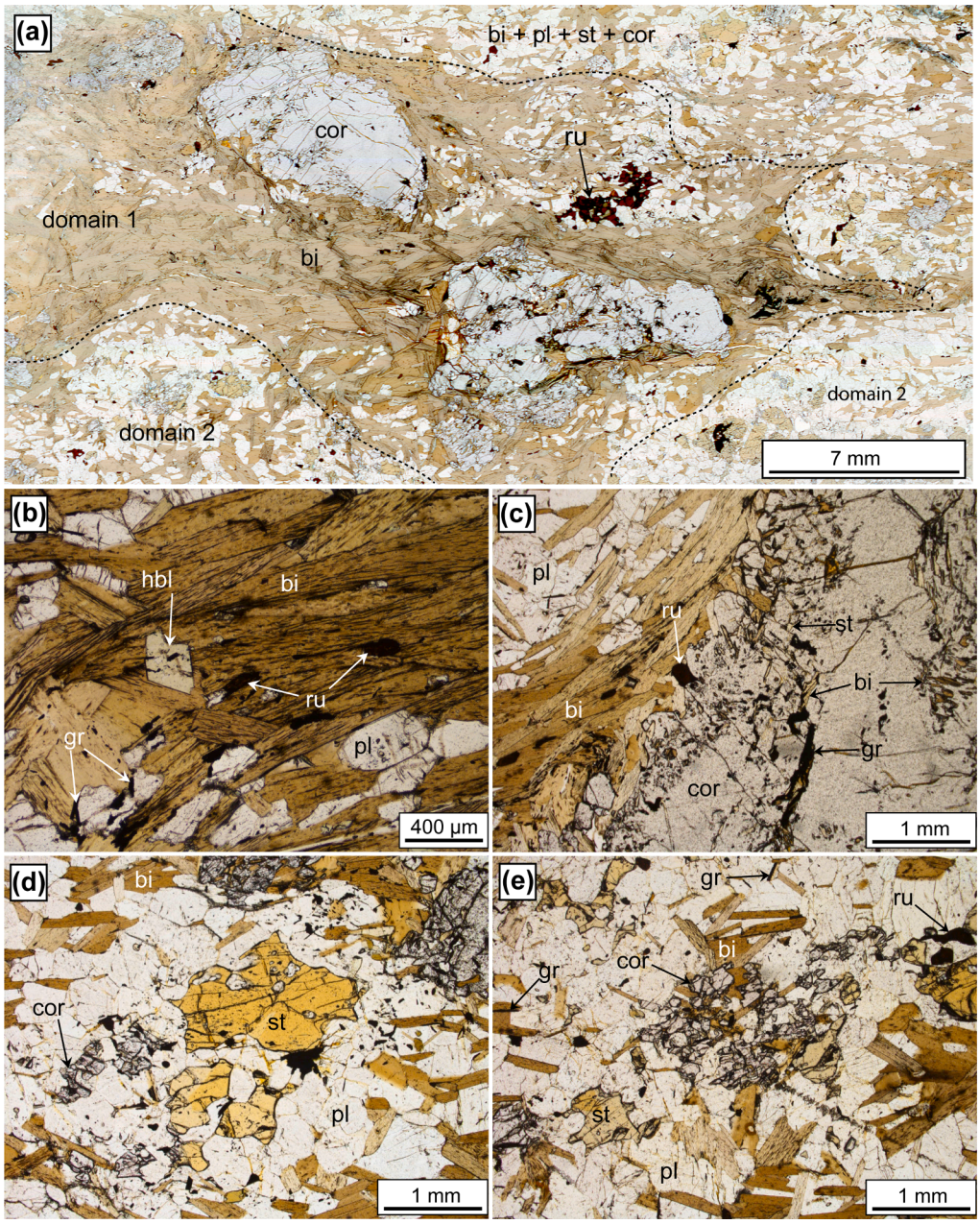

Fig. 3. Photomicrographs of sample 464 (corundum schist). (a) Coarse-grained corundum crystals in biotite-rich domains with a cluster of idioblastic rutile. (b) Rare pale green amphibole in biotite-rich domains. (c) Inclusions of staurolite at the rims of corundum. Graphite and biotite are also included in corundum. (d) Xenoblastic staurolite associated with corundum in a plagioclase-rich domain. (e) Xenoblastic corundum associated with staurolite, rutile, biotite, plagioclase, and graphite. All mineral abbreviations are from Holland and Powell (2011). All photomicrographs are in plane-polarized light. (For interpretation of the references to colour in this figure legend, the reader is referred to the web version of this article.)

4. Methods

4.1. Mineral compositions

Major element compositions of plagioclase, biotite, staurolite, amphibole, tourmaline and corundum from multiple thin sections of corundum schist sample 464 and of aluminosilicate gneiss sample 462 were determined at two different laboratories. Mineral compositions in two thin sections of sample 464 were measured using a JEOL-8200 Electron Microprobe in the Robert M. MacKay Electron Microprobe Laboratory in the Department of Earth Sciences at Dalhousie University. Natural standards were used for calibration. An operating voltage of 15 kV and a beam current of 20nA were used with a ~ 1 μm beam spot. Data were processed with Probe for EPMA. A different thin section of sample 464 and one from sample 462 were analyzed using a JEOL JXA-8200 Electron Microprobe at Copenhagen University. Median values of some of these data are reported in van Hinsberg et al. (2021) and the full dataset is presented here. Operating conditions were a 15 kV accelerating voltage, 15nA beam current and 5 μm spot size. The instrument was calibrated against natural silicate and oxide minerals. The full dataset is presented in the Supplementary Tables S1A and S1B.

A corundum-rich thin section of sample 464 was also analyzed using TESCAN Integrated Mineral Analyzer (TIMA) using a Tescan TIMA3 FEG-SEM at the John de Laeter Research Centre, Curtin University. A full thin section was analyzed to identify the various minerals and their spatial relationships to one another. Operating conditions were a 15 μm working distance, 25 keV beam energy and a 0.05 μm spot size using 4 PulseTor 30 RDX detectors. Pixel sizes are ~ 10 μm by ~ 10 μm.

4.2. Thermobarometry

The Ti-in-biotite thermometer (Henry et al., 2005) is used to determine the estimated temperatures of metamorphism recorded by the matrix assemblages in the aluminosilicate gneiss (sample 462) and the corundum schist (sample 464).

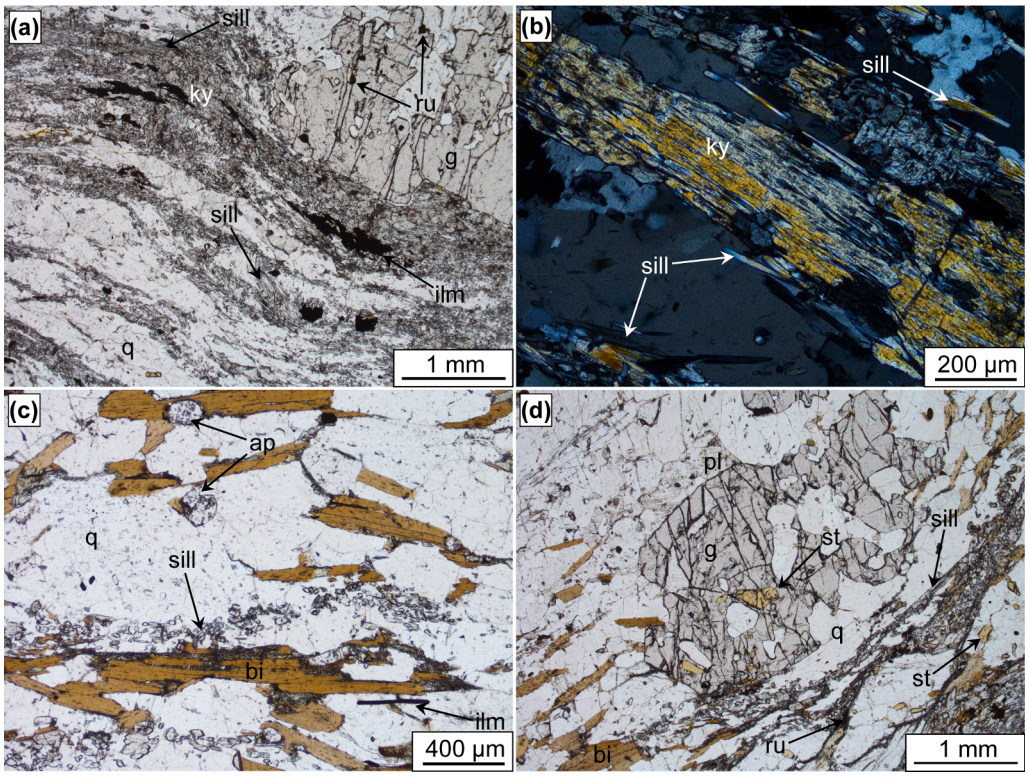

Fig. 4. Photomicrographs of sample 462 (aluminosilicate gneiss). (a) Alternating bands of sillimanite + kyanite (+ilmenite) and quartz wrap around a garnet porphyroblast. Plane-polarized light. (b) Close spatial association of kyanite (twinned crystal) and sillimanite (acicular crystals) within a sillimanite + kyanite-rich band. Cross-polarized light. (c) Biotite + quartz + sillimanite band with fine-grained sillimanite surrounding biotite rims. Plane-polarized light. (d) Garnet porphyroblast with a staurolite inclusion with small staurolite crystals in the surrounding matrix. Plane-polarized light. All mineral abbreviations are from Holland and Powell (2011).

4.3. Fluid compositions

The presence of graphite suggests a mixed CO_2–H_2O fluid may have been present during corundum growth; it is therefore necessary to calculate the composition of an equilibrated fluid to quantify the *P*–*T* conditions of metamorphism. The compositions of fluid present during the growth of the corundum-bearing metamorphic mineral assemblage were modelled in the C–O–H chemical system over a range of temperatures and pressures using the Perple_X suite of thermodynamic modelling programs (Connolly, 2005). The calculations included the fluid species H_2O, CO_2, CO, CH_4, H_2 and O_2, and graphite ± calcite as solids. Calcite occurs in trace quantities in the investigated aluminosilicate gneiss (sample 462), but is absent from the corundum schist (sample 464); the relevance of calcite to the corundum-bearing metamorphic assemblage is unclear. Nevertheless, we model a calcite-absent and calcite-present system to evaluate the sensitivity of fluid compositions to different buffering assemblages. In general, coexisting saturation in calcite and graphite represents a prograde assemblage preserved in the garnet rim of sample 462, whereas graphite saturation reflects the inferred peak metamorphic assemblage of samples 462 and 464. Thermodynamic data for calcite and graphite were taken from the internally consistent data set (ds62) of Holland and Powell (2011). A hybrid equation of state model is implemented for the fluid species (see Connolly, 2005 for details), using the equations of state from Pitzer and Sterner (1994) for H_2O and CO_2, Jacobs and Kerrick (1981) for CH_4, and de Santis et al. (1974) for O_2, H_2 and CO.

4.4. Phase equilibrium modelling

Based on the modelled fluid compositions, forward modelling of metamorphic phase assemblages was used to determine the sensitivity of the observed metamorphic assemblage to fluid composition and to further quantify the *P*–*T* conditions of corundum formation. Modelling was conducted using Theriak-Domino (de Capitani and Brown, 1987; de Capitani and Petrakakis 2010) with the internally consistent data set (ds62) of Holland and Powell (2011). Modelling was conducted in the MnO–Na_2O–CaO–K_2O–FeO–MgO–Al_2O_3–SiO_2–H_2O–TiO_2–Fe_2O_3 (MnNCKFMASHTO) chemical system with the activity–composition models of White et al. (2014a) and White et al. (2014b). This includes the activity–composition model for feldspar from Holland and Powell (2003), for spinel–magnetite from White et al. (2002) and for ilmenite–hematite from White et al. (2000). Quartz, corundum, kyanite, sillimanite, H_2O, and rutile are modelled as pure end members. The bulk composition of sample 464 (corundum schist) is from Yakymchuk and Szilas (2018) and the modelled composition is reported in Table 1. For this sample, 15% of the total amount of iron was assumed to be ferric (c.f. Yakymchuk and Szilas, 2018).

Graphite in the corundum-bearing sample suggests the presence of a mixed fluid (H_2O–CO_2) that cannot be currently combined with activity–composition models for modelling with the Holland and Powell (2011) dataset and the integration of mixed fluids and graphite stability into phase equilibrium modelling is still in its infancy (e.g. Chu and Ague, 2013). To assess the role of H_2O–CO_2 fluids contributing to corundum formation at the Maniitsoq location, we have used an indirect approach by varying the activity of H_2O to values that permit graphite stability and investigating the sensitivity of the predicted corundum-bearing phase assemblage to mixed (i.e. CO_2–H_2O) fluids. Fixing the activity of water to values less than one can be used to qualitatively consider the effects of a mixed COH fluid on corundum stability and this approximates an externally-buffered fluid–rock system. The limitations of this approach are discussed later.

4.5. Carbon-isotope analysis

Six aliquots of graphite from crushed sample 464 were analyzed for carbon isotope ratios at the Queen's Facility for Isotope Research (Queen's University, Canada). Three aliquots were analyzed from the crushed sample and provide the carbon isotope composition of the entire sample. Minor amounts of carbonate may have been present, although no carbonate minerals were observed in thin sections of this sample. So, three additional aliquots of the same crushed sample were treated with HCl and rinsed with deionized water and heated in an oven overnight to

Table 1
Bulk composition used for phase equilibrium modelling (mol%) from Yakymchuk and Szilas (2018).

Sa	SiO_2	Al_2O_3	CaO	MgO	FeO_T	K_2O	Na_2O	TiO_2	MnO	O
464: corundum schist	41.29	15.62	4.08	27.11	5.74	4.30	0.65	0.74	0.04	0.43

remove possible carbonate before analysis; these analyses are the best approximation of the carbon isotope value of graphite. Samples were weighed into tin capsules and the carbon isotopic composition was measured using a Costech ECS 4010 Elemental Analyzer coupled to a Thermo-Finnigan DeltaPlus XP Continuous-Flow Isotope Ratio Mass Spectrometer. $\delta^{13}C$ values are reported using the delta (δ) notation in units of per mil (‰) relative to Vienna Pee Dee Belemnite (VPDB) international standard, with a precision of 0.2‰ and accuracy of 0.1‰ based on analysis of secondary reference materials.

4.6. U–Pb zircon and rutile geochronology

4.6.1. Zircon

Zircon geochronology was conducted on sample 464 to determine the potential provenance of the protolith and evaluate the timing of metamorphism associated with corundum growth. Zircon U–Pb measurements were collected by Laser-ablation inductively-coupled plasma mass spectrometry (LA ICPMS) at the John de Laeter Centre, Curtin University on zircon separated from whole-rock samples. Where possible, multiple spots were collected from both grain cores and rims. For LA ICPMS, ablation was conducted with an excimer laser (RESOlution LR 193 nm ArF with a Lauren Technic S155 cell) with a spot diameter of 30 μm was used with on-sample energy of 2.3 J cm^{-2}, repetition rate of 7 Hz for 45 s for analysis and ~ 60 s of background capture. All analyses were preceded by two cleaning pulses. The sample cell was flushed by ultrahigh purity He (0.68 L min^{-1}) and N_2 (2.8 mL min^{-1}).

U–Pb data were collected on an Agilent 8900 triple quadrupole (QQQ) mass spectrometer with high purity Ar as the carrier gas (flow rate 0.98 L min^{-1}). Analyses of every 10 unknowns were bracketed by analyzing a standard block containing the primary zircon reference materials GJ-1 (608.5 ± 1.5 Ma; Jackson et al., 2004) and OG1 (3465.4 ± 0.6 Ma; Stern et al., 2009), which were used to monitor and correct for mass fractionation and instrumental drift. The standard block also contained a range of secondary zircon standards spanning Archean to Phanerozoic ages, including Plešovice (337.13 ± 0.37 Ma; Sláma et al., 2008), 91,500 (1062.4 ± 0.4 Ma; Wiedenbeck et al., 1995) and Maniitsoq (3008.70 ± 0.72 Ma; Marsh et al., 2019; all uncertainties at 2 s), which were used to monitor data accuracy and precision. During the analytical sessions, Plešovice (336 ± 2, n = 10, MSWD = 2.2), GJ-1 (605 ± 2, n = 15, MSWD = 0.25), 91,500 (1063 ± 7, n = 15, MSWD = 2.5), Maniitsoq (3009 ± 7, n = 10, MSWD = 2.0), and OG1 (Mean = 3465 ± 3 , n = 15, MSWD = 0.73), yielded weighted mean ages ($^{238}U/^{206}Pb$ ages for those reference materials under 1600 Ma) within 2 s of the accepted age (Supplementary Table S2), when reduced using appropriate matrix-matched primary reference material.

Data were reduced in Iolite (Paton et al., 2011) and in-house Excel macros. Zircon analyses are considered concordant when the $^{207}Pb/^{206}Pb$ and $^{206}Pb/^{238}U$ ages are within 10% of each other. Uncertainties on the primary reference materials were propagated in quadrature into the unknowns and secondary zircon reference materials. Age calculations and plots use Isoplot 4.15 software (Ludwig 2012). Full isotopic data for the samples are given in Supplementary Table S3. Common-Pb was not corrected as all concordant analyses have < 0.1% f206%. All spot analyses are presented at 2 s (unless specified otherwise) and weighted mean analyses are given at 95% confidence.

LA ICPMS analyses also included analyses of select trace elements. Each element was monitored for 0.01–0.02 s each (^{29}Si, ^{49}Ti, ^{89}Y, ^{90}Zr, ^{91}Zr, ^{93}Nb, ^{178}Hf, ^{204}Pb, ^{206}Pb, ^{207}Pb, ^{208}Pb, ^{232}Th, ^{238}U). The in-house zircon standard PL-1 (megacryst of Penglai zircon; Li et al., 2010) was used as the primary standard to calculate elemental concentrations (using ^{91}Zr as the internal standard element and assuming 43.14% Zr in the unknown zircon). During the time-resolved analysis, contamination from inclusions and compositional zoning were monitored and only the relevant part of the signal was integrated. The trace element results for NIST 612 (secondary standard), using NIST 610 as the reference material and assuming 33.6% Si, indicate that the accuracy was better than 3% for most elements. The time-resolved mass spectra were reduced using the Trace Elements data reduction scheme in Iolite 3.5 (Paton et al., 2011).

4.6.2. Rutile

Rutile U–Pb measurements were collected during two sessions at the GeoHistory Facility, John de Laeter Centre, Curtin University. The excimer laser used in ablation was the same as that for zircon (RESOlution LR 193 nm ArF with a Lauren Technic S155 cell) with spot diameter of 22 μm was used with on-sample energy of 2.4 J cm^{-2}, repetition rate of 7 Hz for 45 s of total analysis time and ~ 60 s of background capture. All analyses were preceded by two cleaning pulses. The sample cell was flushed by ultrahigh purity He (0.68 L min^{-1}) and N_2 (2.8 mL min^{-1}).

In session one U-Pb data were collected on a Nu Plasma II multi collector mass spectrometer, whereas in session two an Agilent 8900 triple quadrupole mass spectrometer was used; in both sessions, rutile was analysed directly in thin section to maintain petrographic context. Analyses of reference material was made every 10 unknowns. Standard material included rutile reference materials R10 (Luvizotto et al., 2009) and Wodgina (Ewing, 2011). Most ^{208}Pb in rutile cannot be derived from radioactive decay of ^{232}Th within the mineral due to the low Th content. Hence, common Pb was calculated by measuring ^{208}Pb and using this isotope as a monitor of common Pb. The radiogenic Pb component in ^{206}Pb and ^{207}Pb was calculated from the measured $^{206}Pb/^{208}Pb$ and $^{207}Pb/^{208}Pb$ ratios referenced to the expected ratio from a Pb evolution model of Stacey and Kramers (1975) for the expected age of the material. The corrected ^{206}Pb and ^{207}Pb count rates were then used to calculate $^{207}Pb/^{206}Pb$ and $^{206}Pb/^{238}U$. Rutile R10 (1090 ± 5 Ma; Luvizotto et al., 2009) was used as the primary reference material with Wodgina (2846 ± 8 Ma; Ewing, 2011) used to verify the analytical and reduction process. During the first analytical session Wodgina yielded a Concordia age of 2832 ± 12 Ma (MSWD = 1.5; n 12), during the second session Wodgina yielded a Concordia age of 2831 ± 17 Ma (MSWD = 2.2, n = 9). Data were reduced in Iolite (Paton et al., 2011) and in-house Excel macros in a similar fashion to zircon except as previously stated 208 correction was applied.

5. Results

5.1. Mineral compositions

Mineral compositions from the corundum schist (sample 464) are summarized in Fig. 5 and the complete data set is presented in Supplementary Tables S1A and S1B. Plagioclase has X_{An} (molar Ca/ [Ca + K + Na]) values between 0.90 and 0.95 and there is no apparent core–rim zoning nor variability in compositions across the investigated samples. Biotite has Mg# (molar Mg / [Mg + Fe]) values between 0.72 and 0.77 and is compositionally homogeneous throughout microstructural

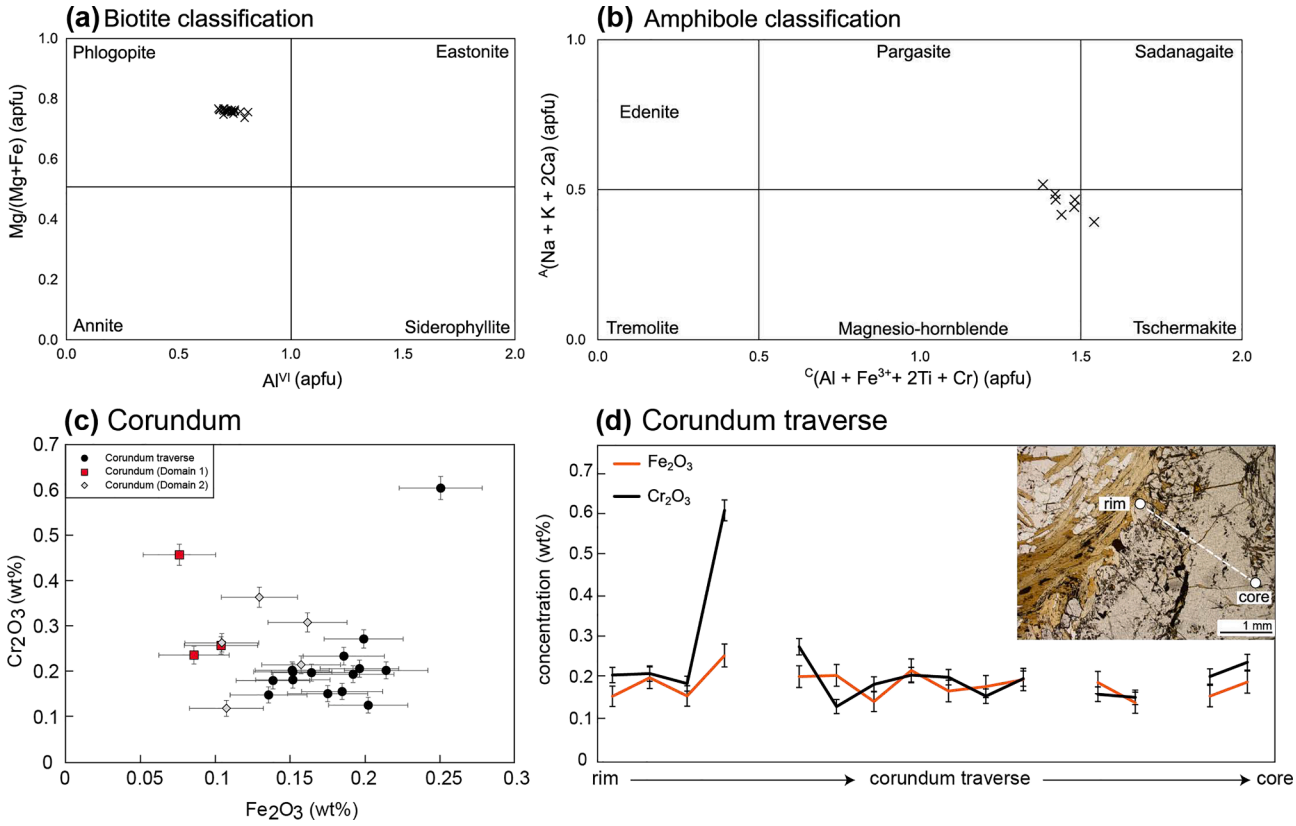

Fig. 5. Mineral composition data for the corundum schist (sample 464). (a) Biotite classification diagram with measured compositions (after Deer et al., 1992). (b) Amphibole classification diagram with measured compositions (modified after Hawthorne et al., 2012). (c) Corundum composition diagram. (d) Compositional transect (2.5 mm in length) from rim to core through a large (~1 cm wide) corundum grain. Blank spaces represent analyses that were rejected due to low totals. Concentrations of Fe_2O_3 do not show significant variation and Cr_2O_3 concentrations are low except for one point near the rim.

domains (Fig. 5a). Biotite also has negligible amounts of Cl and F. Biotite inclusions in corundum have similar compositions to biotite in the matrix. Staurolite has Mg# from 0.34 to 0.36 in the matrix. Inclusions of staurolite (~85 μm) in corundum and have Mg# of 0.24–0.26. Amphibole is compositionally homogeneous throughout the sample and has Mg# from 0.67 to 0.69. Based on the classification of Hawthorne et al., (2012), the amphibole is of the calcic sub-group and is mainly classified as magnesio-hornblende (Fig. 5b). Tourmaline has Mg# values that range from 0.85 to 0.87. All measured FeO in corundum was determined to be Fe_2O_3 based on stoichiometry using the method of Droop (1987). Concentrations of Fe_2O_3 in domain 1 and domain 2 corundum are all < 0.25 wt% (Fig. 5c). One transect across a large corundum crystal shows negligible zoning of Fe_2O_3 (Fig. 5c). With the exception of one analysis near the rim of the large corundum crystal that yielded a Cr_2O_3 concentration of 0.6 wt% (Fig. 5d), all other analyses of corundum give concentrations between 0.12 and 0.46 wt%.

Mineral compositions from the aluminosilicate gneiss (sample 462) are presented in Supplementary Table S1B and are summarized here. Plagioclase has X_{An} values that vary from 0.84 to 0.88; these are more Na-rich than plagioclase from the corundum schist. Biotite has Mg# values that range from 0.67 to 0.76 and these are similar to those from the corundum schist, but extend to lower values. Biotite contains up to 0.20 wt% fluorine and chlorine was not measured. Staurolite has Mg# of 0.21–0.31, which is lower than the Mg# of staurolite from the corundum schist. Garnet is almandine-rich with negligible zoning and X_{Fe} (molar Fe / [Fe + Mg + Ca + Mn]) values range from 0.67 to 0.72. Tourmaline shows minimal variation in composition with Mg# between 0.73 and 0.76, which is significantly lower than tourmaline from the corundum schist (Table S1A). In general, ferromagnesian minerals (biotite, tourmaline, staurolite) are more Mg-rich in the corundum schist compared with those in the aluminosilicate gneiss. This probably reflects the more magnesian whole-rock composition of the corundum schist (Mg# = 0.83) compared with aluminosilicate gneiss (Mg# = 0.30) (c.f. Yakymchuk and Szilas, 2018).

5.2. Thermobarometry

The results of mineral thermometry for samples 462 and 464 are summarized in Fig. 6. The Ti-in-biotite thermometer yielded a median temperature of ~ 635 °C ($n = 26$) for the aluminosilicate gneiss (sample

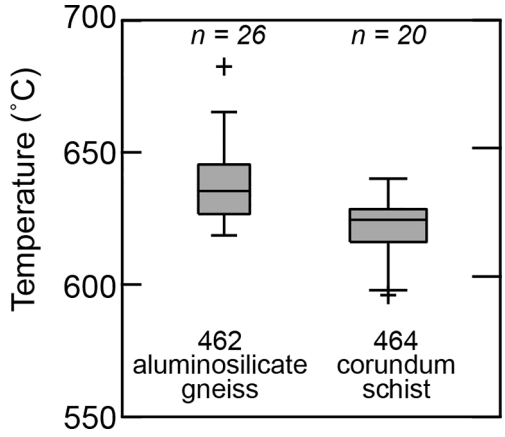

Fig. 6. Results of mineral thermometry. The box and whisker plots represent temperature estimates from the Ti-in-biotite thermometer ($n = 26$ for sample 462; $n = 20$ for sample 464). The boxes represent the interquartile range, the whiskers extend to the furthest data point within 1.5 times the interquartile range and the crosses are outside this range.

462) and a slightly lower median temperature of ~620 °C ($n = 20$) for the corundum schist (sample 464). Considering the uncertainty associated with mineral thermometers at high temperatures (e.g. Powell and Holland, 2008), these estimates are considered to be within uncertainty of each other.

5.3. Fluid compositions

Fluid compositions were determined to assess the importance of mixed hydrous–carbonic fluids in the stability of corundum and provide constrains for phase equilibrium modelling. Calculated fluid compositions in equilibrium with the carbon-bearing minerals are summarized in Fig. 7. Graphite is inferred to be part of the peak metamorphic paragenesis whereas it is unclear if calcite was present at the metamorphic peak. For all scenarios, H_2O is the dominant fluid species (Fig. 7a–d). For fluids in equilibrium with calcite and graphite, the proportion of CO_2 is estimated to increase with temperature from < 5 mol.% at 600 °C to 14–18 mol.% at 700 °C. For fluids in equilibrium with graphite, CH_4 is predicted to reach molar proportions of ~5%. The amount of CO and H_2 in the calculated fluid compositions is negligible (Fig. 7).

5.4. Phase equilibrium modelling

Two sets of phase diagrams are used to investigate the petrogenesis of the corundum-bearing rocks. Together, the results are used to evaluate the potential involvement of mixed hydrous–carbonic fluid associated with the growth of metamorphic corundum.

We evaluate the stability of corundum as a function of water activity using a temperature–a_{H2O} diagram constructed at 7 kbar (c.f. Yakymchuk and Szilas, 2018; van Hinsberg et al., 2021) for the bulk composition of sample 464 and the results are shown in Fig. 8. Corundum is predicted to be stable over a ~ 50–100 °C interval for a_{H2O} between 0.25 and 1. Corundum is expected to be stable at lower temperatures with lower water activities. In addition to corundum, the peak metamorphic assemblage inferred from petrographic observations includes biotite,

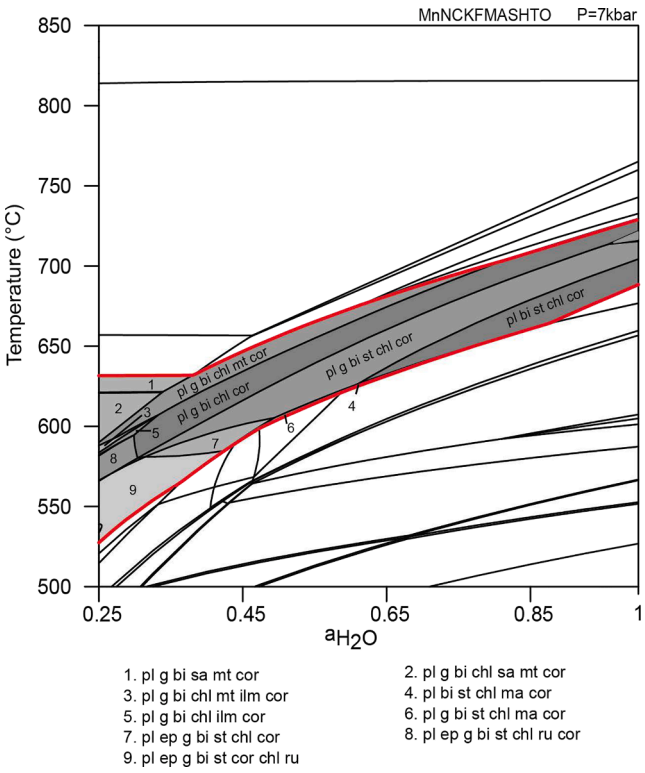

Fig. 8. Temperature–a_{H2O} diagram calculated at 7 kbar showing the modelled stability of corundum and other minerals. Values along the abscissa represent the activity of H_2O (relative to free H_2O) that represent a relatively CO_2-rich fluid at low values up to water saturation at 1.0. The temperature of modelled corundum stability decreases for lower activities of H_2O. Epidote is not observed in the sample, but it is predicted at $a_{H2O} < 0.5$. The fully labelled diagram is presented in the supplementary material. Mineral abbreviations from Holland and Powell (2011).

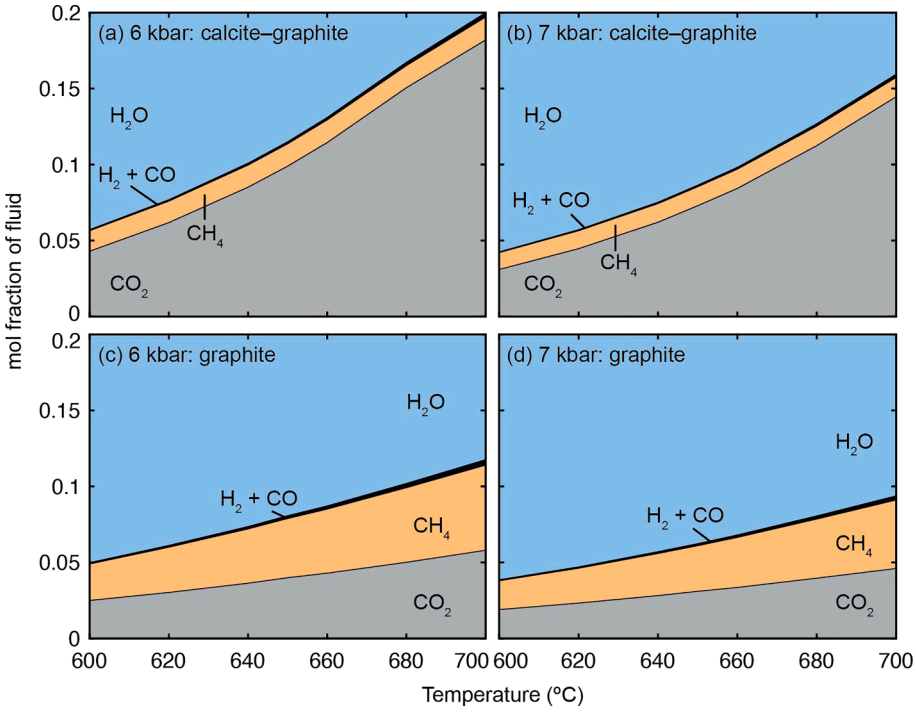

Fig. 7. Calculated fluid compositions in equilibrium with calcite and graphite (a,b) and with graphite (c,d) as a function of temperature and pressure. For all fluid compositions, H_2O is the dominant species.

plagioclase, and staurolite as well as accessory rutile, graphite, tourmaline and hornblende. The mode of hornblende in the corundum schist is ≪1 vol% and is excluded from further discussion. Tourmaline cannot be quantitatively modelled and its low abundance is considered within uncertainty of the modelling. Epidote is predicted in the model to be stable with corundum for a fluid composition of $a_{H2O} < 0.5$. Given that epidote was not observed in the sample, we use a value of 0.5 as a lower estimate of the activity of H_2O in the system. Staurolite, plagioclase, biotite and corundum are predicted to be stable together at $a_{H2O} > 0.35$. However, chlorite and garnet are also predicted to be stable with this assemblage over most of the modelled range of a_{H2O} values, and these minerals are not present in sample 464. The exception is a narrow field from $a_{H2O} = 0.60–1.0$ that does not have garnet present, but chlorite is predicted to be stable for all corundum-bearing fields. The presence of chlorite in the model despite the absence of this mineral from the corundum schist is explored later.

A second set of diagrams shows the predicted phase assemblages for the same corundum schist (sample 464) as a function of pressure and temperature for two different externally buffered fluid compositions based on the results presented in Fig. 8. The predicted phase stability fields for the H_2O-saturated composition are shown in Fig. 9a and those for $a_{H2O} = 0.5$ are shown in Fig. 9b.

For the model with $a_{H2O} = 1$, the stability of corundum is restricted to > 3 kbar and > 640 °C (Fig. 9a). Staurolite is predicted to be stable from ~ 5.5–9 kbar and 650–730 °C. At lower pressures and higher temperatures, sapphirine is predicted to be stable. Garnet stability is restricted to > 5 kbar and > 650 °C. Chlorite (high Mg) is predicted to be stable up to 750 °C. Orthopyroxene is restricted to > 650 °C at low pressures. Rutile is restricted to < 630 °C over the range of modelled pressures. The estimated solidus is at 700–850 °C with decreasing pressure from 12 to 8 kbar. There is no stability field for the observed mineral assemblage inferred to be in equilibrium with corundum. The stability fields of corundum and staurolite overlap at 6–7.5 kbar and ~ 700 °C, however this also includes chlorite, which is not observed in thin section.

For the model with $a_{H2O} = 0.5$, the stability field of corundum is extended to 550 °C and 1 kbar (Fig. 9b). Cordierite is restricted to < 4–5 kbar with increasing temperature in the stability field of corundum, which restricts the pressure of equilibration to higher pressures. Staurolite is restricted in the corundum stability field from 550 to 620 °C and up to higher pressure. Staurolite and corundum are predicted to be stable together outside the stability field of garnet from 4 to 6 kbar and 560–600 °C. Rutile is restricted to < 600 °C in the stability field of corundum (Fig. 9b). Again, chlorite is predicted to be stable in the modelling (Fig. 9b), but it is not inferred to be part of the peak metamorphic assemblage that includes corundum.

5.5. Carbon isotopes

Carbon isotopes are used to assess the source of carbon that was present in the inferred hydrous-carbonic fluid that equilibrated with graphite. The results of carbon isotope analysis of graphite from the corundum schist (sample 464) are summarized in Table 2. Untreated sample aliquots yield $\delta^{13}C$ values that vary from –14.2 to –17.2 ‰ whereas the acid-treated samples yielded values ranging from–13.3 to –15.7 ‰. The variability indicates some carbon isotopic heterogeneity in

Table 2
Results of carbon isotope analysis.

Sample replicate	$\delta^{13}C$ (VPDB; ‰)
464 HCl treated 1	–13.4
464 HCl treated 2	–13.3
464 HCl treated 3	–15.7
464 Untreated 1	–17.2
464 Untreated 2	–15.1
464 Untreated 3	–14.2

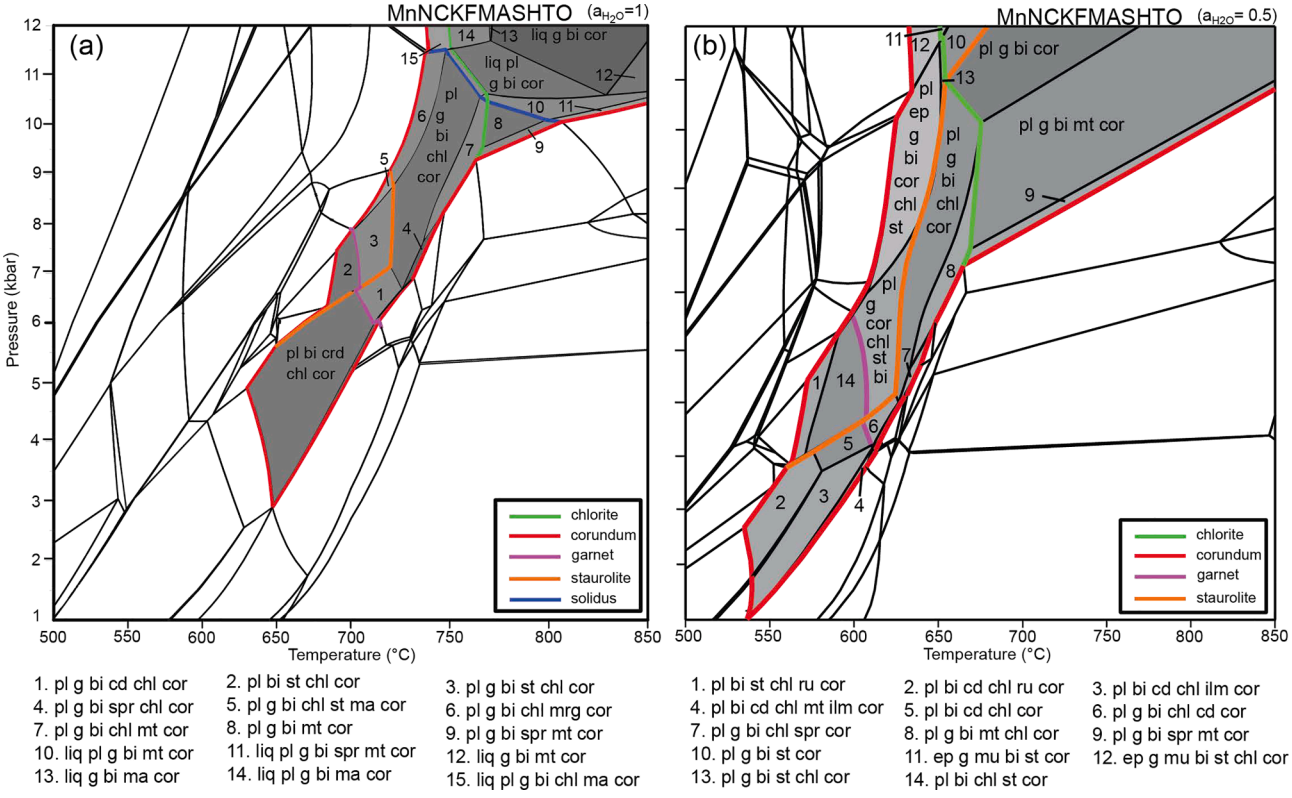

Fig. 9. Pressure–temperature diagram for corundum-schist (sample 464) for (a) $a_{H2O} = 1$, and (b) $a_{H2O} = 0.5$. The predicted P–T stability field of corundum is larger at reduced water activity. The fully labelled diagrams are presented in the supplementary material. Mineral abbreviations from Holland and Powell (2011).

the corundum schist. Nonetheless, these values are within the range of organic carbon (Schidlowski, 1987; 2001), but, given the potential for carbon isotope fractionation during high-temperature metamorphism, it is unclear if these values represent bona fide organic signatures or fractionation of a non-biogenic source (e.g. Ohtomo et al., 2014). This is explored in the discussion.

5.6. U–Pb zircon and rutile geochronology

5.6.1. Zircon

Zircon crystals in sample 464 are sub-rounded to sub-angular and have low to moderate length to width ratios of 1:1 to 4:1. Six analyses are > 5% discordant and a further seven analyses are core-rim mixtures or situated on cracks or inclusions and are not considered further (Group D). Two analyses (Group P) with faded and mottled internal textures with high U (1052–1263 ppm) yield $^{207}Pb/^{206}Pb$ dates of *c.* 2.59 to 2.58 Ga, interpreted as having experienced minor ancient radiogenic Pb-loss. Twenty-three analyses (Group S) were conducted on grains with a variety of internal textures, including bright, oscillatory-zoned cores and weakly-developed oscillatory- and sector-zones but importantly lacking fading or mottling. These analyses yield $^{207}Pb/^{206}Pb$ dates between *c.* 3.13 and 2.86 Ga (Fig. 10a). The 23 analyses in Group S yield dates that define significant age components at *c.* 3.03 and 3.07 Ga, and several minor components within the range *c.* 2.95–3.11 Ga. These ages are interpreted as the ages of zircon-crystallizing rocks in the detrital source region(s). The youngest analysis in Group S yields an age of 2861 ± 15 Ma, which is interpreted as the maximum depositional age for the sample. Twelve analyses (Group M) sited on either discrete homogenous grains or low CL response rims yield $^{207}Pb/^{206}Pb$ dates between *c.* 2.72 and 2.60 Ga. These analyses yield high to very high concentrations of U (605–1324 ppm), and likely reflect, to differing degrees, either or both of partial radiogenic-Pb loss of pre-existing cores and neoblastic metamorphic growth. New growth for at least a component of Group M is implied by the distinct trace element compositions in comparison to Group S, which is enriched for some elements (Supplementary Table S3). Relative to Group S, Ti is enriched (average 36 ppm in Group M versus 20 ppm in Group S), Y is depleted (average 891 ppm versus 1031 ppm), Nb is depleted (average 1 versus 2 ppm), Yb enriched (445 ppm versus 283 ppm), and Hf enriched (11198 versus 9706 ppm). The full suite of zircon analytical results is presented in Supplementary Table S2.

5.6.2. Rutile

Session 1 using the MC-ICP-MS targeted ~ 40 rutile grains across a thin section of sample 464 (Fig. 10b) whereas Session 2 using the QQQ-ICP-MS targeted a single rutile inclusion in corundum in sample 464 with a grid pattern of ablation spots (Fig. 11) to produce an age map of a single rutile grain. Both the QQQ-ICP-MS and MC-ICP-MS analyses of matrix rutile yield similar results that scatter close to or just to the right of the inverse concordia curve (e.g. minor normal discordance) and yield $^{207}Pb/^{206}Pb$ ages between *c.* 2.5–1.7 Ga (Fig. 10b). Sixteen analyses (Group D) indicate measurable Th—principally in inclusions—and cannot be corrected for common Pb using measured ^{208}Pb; these analyses are not considered further (mixed analyses in Fig. 10b). The remaining 79 analyses define a free regression line that intersects the concordia curve at 2503 ± 58 Ma and 1517 ± 44 (MSWD = 1.8). The upper intercept of 2503 ± 58 Ma is within uncertainty of the oldest, most precise, concordant analysis that yields a $^{207}Pb/^{206}Pb$ age of 2447 ± 21 Ma (1 s). The upper intercept is interpreted as the best estimate for the age of rutile growth. The spread of ages to a lower intercept of *c.* 1.5 Ga is interpreted to record continuous Pb diffusion above the Pb blocking temperature in rutile and is not afforded geological significance as a single age, as radiogenic Pb is interpreted to have dissimilar susceptibility to diffusion within different rutile domains (Kooijman et al., 2010). A further examination of the closure temperature of rutile is presented in the discussion. A minor amount of recent Pb loss may also be inferred for some of the analyses based on the distribution of the rutile data slightly to the right of concordia curve in Fig. 10b. The full suite of rutile analytical results is presented in Supplementary Table S4.

6. Discussion

6.1. Limitations of thermobarometry and phase equilibrium modelling

The use of thermobarometers requires the assumption of equilibrium in the metamorphic assemblage, which is troublesome for cation exchange thermometers that can re-equilibrate during cooling after the metamorphic peak (Frost and Chacko, 1989; Spear and Florence 1992; Powell and Holland, 2008). An additional complication is that the corundum schist has heterogeneous mineral assemblages. For example, minor hornblende is present in some thin sections and not in others and tourmaline is heterogeneously distributed with large grains (~3 mm) associated with corundum and is generally absent from biotite–plagioclase domains. Although mineral assemblages are heterogeneous, matrix mineral compositions are generally similar across sample

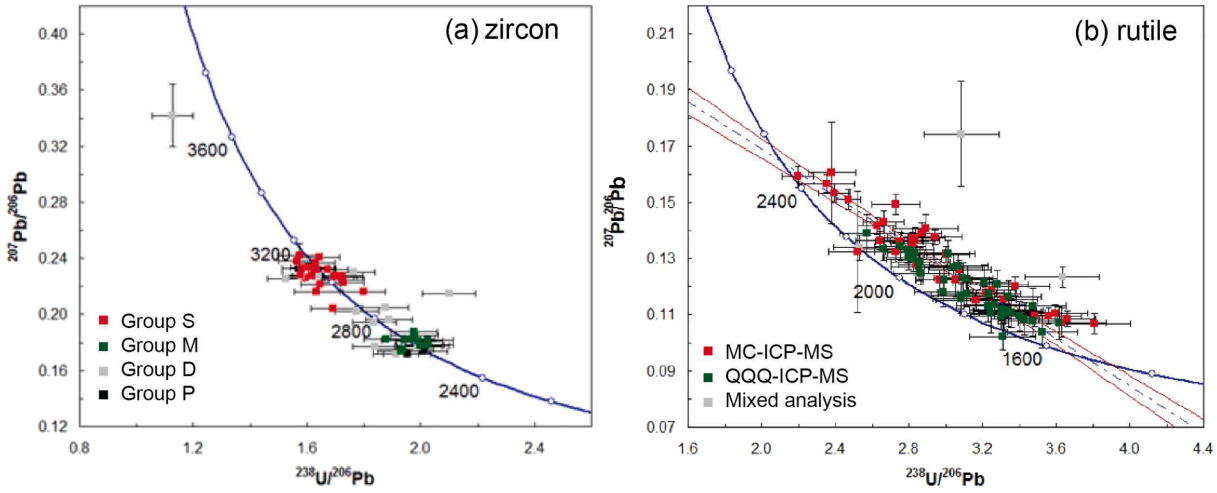

Fig. 10. (a) U–Pb analytical data for zircons from sample 464: corundum-schist. Group S is detrital zircon. Group D are discordant or mixtures. Group M are metamorphic or affected by metamorphic processes. Group P have experienced radiogenic-Pb loss but are concordant. (b) U–Pb analytical data for rutile. Grey squares are mixtures where analysis sampled non-rutile minerals. All shown analyses have a ^{208}Pb correction (no Th). All uncertainty crosses are at 2 s.

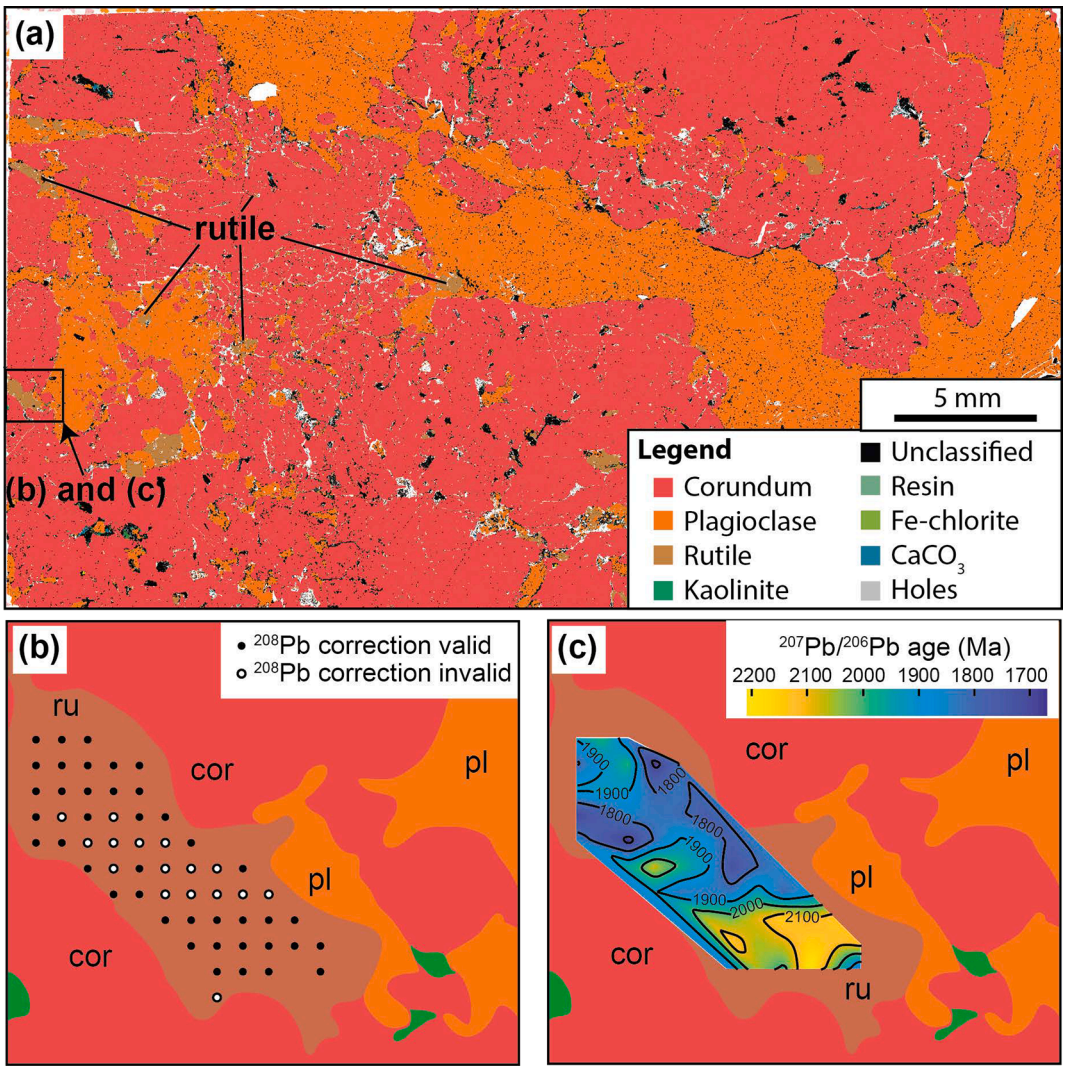

Fig. 11. (a) TIMA image of thin section with important mineral identified for sample 464. Rutile occurs at grain boundaries between corundum and plagioclase; some smaller grains are also inclusions in plagioclase. (b) Locations of analyses on rutile grain on simplified TIMA image. (c) Contours of $^{207}Pb/^{206}Pb$ ages (all data points) overlain on simplified TIMA image. Higher $^{207}Pb/^{206}Pb$ ages at the end of the grain neighbouring plagioclase and a general pattern of apparent reducing ages towards the rim.

464 (Fig. 5) and 462 (Supplementary Table S1B) and permit the use of thermobarometers.

Temperature estimates from the various thermometers yield different values. The Henry et al. (2005) Ti-in-biotite thermometer is based on equilibration pressures of 4–6 kbar and was calibrated for mostly quartz-present assemblages. The similarity between temperature estimates from the aluminosilicate gneiss (sample 462) and the corundum schist (sample 464)—that were inferred to have equilibrated at similar *P–T* conditions—suggests that the presence or absence of quartz did not have a major effect on the estimated temperatures. The general agreement in estimated temperatures between the Ti-in-biotite thermometer and the results of phase equilibrium modelling suggests that the rocks record peak metamorphism at ~ 650 °C. Nevertheless, the estimated temperatures of metamorphism and corundum formation are lower than those predicted by Yakymchuk and Szilas (2018) on the same samples.

Phase equilibrium modelling of the two samples is also hindered by the heterogeneous mineral assemblages, and for the corundum schist, the refractory composition. The corundum-bearing rock (sample 464) is Mg-rich and silica-undersaturated, which is very different from the metapelite compositions used to calibrate and assess the suitability of the activity–composition models (e.g. White et al., 2014a, b) used with the Holland and Powell (2011) database. Hence, it is reasonable to acknowledge that the absolute *P–T* conditions may have moderate uncertainties, but the topology of the diagrams (i.e. relationships between the various fields) are probably more robust (e.g. Powell and Holland, 2008), and geological insight can thus be obtained from them. In addition, the heterogeneous distribution of minerals and variable modes in different microstructural domains preclude us from using modal proportion calculations (e.g. isopleths) to refine these *P–T* estimates from the phase diagrams. Even an assessment of local effective bulk composition is not useful for our samples considering: (i) the textural heterogeneity of the corundum schist in 3 dimensions (i.e. in thin section and outside the plane of the thin section), (ii) the different mobilities of components during metamorphism (e.g. mobile H_2O versus relatively immobile Al_2O_3 or even SiO_2 in quartz-absent rocks) resulting in variably flattened chemical potential gradients in 3 dimensions (c.f. Powell et al., 2019), and (iii) that effective bulk composition is expected to change during cooling (e.g. Stüwe, 1997). Keeping these limitations in mind, we use phase equilibrium modelling to provide a first-order estimate of the peak *P–T* conditions; the similarities between the results of thermobarometry and the modelling suggest that these are complementary and appropriate approaches for the corundum schist (sample 464).

Mixed fluids associated with graphite may be complex mixtures of H_2O and CO_2 as well as CH_4, H_2, and CO components (e.g. Ohmoto and Kerrick, 1977). Our metamorphic phase equilibrium modelling approach does not consider the specific composition of the fluid, but only permits us to investigate an imposed (i.e. buffered) water activity on the system. The modelled composition of a fluid in equilibrium with graphite and calcite at the estimated *P–T* conditions includes up to ~ 20 mol% CO_2, and up to ~ 5 mol% CO_2 for a graphite-only buffer (Fig. 7). Although CO_2–H_2O fluids exhibit non-ideal behaviour, water activities are not expected to be drastically different. Consequently, the results of our modelling between $a_{H2O} = 1$ and $a_{H2O} = 0.5$ (Figs. 8, 9) are considered appropriate.

Garnet is predicted to be stable over a wide range of *P–T* conditions, but no garnet was observed in the corundum-bearing sample. The inclusion of Mn in the modelled compositional system tends to stabilize garnet at lower *T* and lower *P* conditions than normally observed, and this is attributed to the lack of Mn activity–composition models for some of the other minerals in the system. Although the modal amount of garnet predicted by the modelling is expected to be limited—<4 vol% in the stability field of staurolite in the H_2O-saturated system—we do acknowledge that this inconsistency may have an effect on the absolute *P–T* conditions calculated. Nonetheless, the presence of staurolite in the matrix is consistent with amphibolite-facies conditions.

There are three other discrepancies between the modelling results and the observed mineral assemblage. First, a minor (<1 vol%) amount of hornblende is present in sample 464, but it is not included in the modelling due to the current incompatibility of amphibole activity–composition models with the most recent set of activity–composition models for aluminous metasedimentary rocks (e.g. White et al., 2014a, b). Second, there is a minor amount (up to ~ 10 vol%) of chlorite predicted by the phase equilibrium modelling, but no chlorite is observed in thin section for sample 464, and there is more biotite in the sample (>60 vol%) than predicted by phase equilibrium modelling (~50 vol%). The modelled bulk composition may have less potassium than needed to predict the observed proportion of biotite; we speculate that chlorite is an alternative repository for Fe and Mg in the modelling. Third, the absence of boron from the modelled chemical system prohibits us from including tourmaline (e.g. van Hinsberg and Schumacher, 2007) in the calculations, which may be important in microstructural domains that host some of the corundum. This may influence the estimated stability field of ferromagnesian and aluminosilicate minerals. The corundum schist is heterogeneous at the scale of a hand sample and this may account for some of these discrepancies. With these necessary simplifications and apparent discrepancies in mind, we now discuss a potential *P–T* history of the corundum schist sample from the Maniitsoq region.

6.2. *P–T conditions of corundum growth*

Phase equilibrium modelling of sample 464 suggests that an assemblage of staurolite, corundum, biotite and plagioclase was stable at ~ 670–700 °C at 6–7 kbar for a water-saturated ($a_{H2O} = 1$) system. However, rutile and corundum are not expected to be stable together in a water-saturated system. The modelling also predicts chlorite at these *P–T* conditions, but this mineral was not observed in thin section. For a system with a reduced activity of H_2O ($a_{H2O} = 0.5$), an assemblage of corundum, staurolite and rutile (in addition to biotite and plagioclase) is predicted to be stable at ~ 550–600 °C at 4–6 kbar. Rutile may have been stable at higher temperatures based on the oxidation state of the system during heating (e.g. White et al., 2000; Diener and Powell 2010); therefore, we consider the temperatures estimated from the estimated stability fields of rutile and corundum to be a minimum. Ti-in-biotite thermometry yields temperatures of ~ 600–650 °C (Fig. 7), which are between the predicted stability fields of corundum for the water-saturated ($a_{H2O} = 1$) and reduced water activity ($a_{H2O} = 0.5$) models. Considering the uncertainties in the modelling and the minor discrepancy between the observed and modelled metamorphic mineral assemblages, the best estimate for the peak metamorphic conditions associated with the corundum-bearing assemblage is ~ 600–700 °C at ~ 4–7 kbar. These *P–T* conditions are compatible with peak estimates of ~ 6.5 kbar at ~ 650 °C from the inferred precursor aluminosilicate gneiss and for a modelled domainal bulk composition (e.g. using mineral modes and median mineral compositions) of the ruby-bearing schist (van Hinsberg et al., 2021).

The estimated peak metamorphic temperatures for the corundum schist here are somewhat lower than those predicted by Yakymchuk and Szilas (2018), who inferred that corundum growth at $T > 700$ °C, but did not consider the presence of mixed H_2O–CO_2 fluid. The prograde history of the corundum schist is not clear. A single measurement of a staurolite inclusion in corundum has a lower Mg# than the matrix staurolite; in general, the Mg# of staurolite is generally expected to increase with prograde metamorphism (e.g. Albee, 1972), although this is not always the case (McLellan, 1985). However, we cannot determine from this if the prograde history accompanied compression or was isobaric. Furthermore, the microstructural inference of sillimanite growth after kyanite (Fig. 4b) can occur during isobaric heating or heating accompanying compression. Nonetheless, corundum is expected to be part of the peak metamorphic assemblage (Fig. 9).

The development of a silica-undersaturated aluminous rock that can stabilize corundum in the Maniitsoq region was proposed by Yakymchuk and Szilas (2018) to be the product of metasomatism associated with the juxtaposition of low a_{SiO2} ultramafic rocks against high a_{SiO2} aluminous gneiss. The transfer of SiO_2 and K_2O between these two rock types was facilitated by fluids, which resulted in formation of amphibole in the adjacent ultramafic rocks (Yakymchuk and Szilas, 2018). This fluid was probably acidic, reduced, boron-rich, with high K/Na, and may have been sourced from late-orogenic magmatism (van Hinsberg et al., 2021). Our modelling indicates peak metamorphism at ~ 600–700 °C; at these temperatures, corundum is expected to be stable in both water-saturated systems (Fig. 9a) and systems with a mixed fluid (Fig. 9b), however corundum is only expected to be stable with rutile in the H_2O-undersaturated system, which better reflects our inferred paragenesis.

The H_2O–CO_2 composition of the fluid associated with the corundum-bearing assemblage is constrained by the presence of key minerals (e.g. graphite) and the composition of hydrous minerals. Biotite has negligible (<0.1 wt%) concentrations of Cl and F (Supplementary Table S1). Minor graphite and calcite are present in the inferred protolith (aluminosilicate gneiss, sample 462) and suggests that the carbon may have been locally sourced. The sampled corundum-bearing horizon contains proportionally more graphite and may have had a slightly different protolith compared with the immediately adjacent aluminosilicate gneiss. Nonetheless, a mixed H_2O–CO_2 fluid was present during the growth of the peak metamorphic assemblage that includes corundum. This fluid was necessary to facilitate the metasomatic transfer of SiO_2 out of—and movement of Cr into—the precursor to the corundum schist that enabled corundum growth in a quartz-undersaturated system (e.g. Yakymchuk and Szilas, 2018; van Hinsberg et al., 2021).

6.3. *Source of carbon*

Graphitic carbon is associated with corundum at the Maniitsoq occurrence and it has a key effect on buffering fluid composition that facilitated corundum growth at amphibolite-facies conditions. However, whether the carbon was locally or externally sourced will influence what rock types can host corundum, i.e. is a carbon-rich protolith necessary for amphibolite-facies corundum growth in similar rocks to those at Maniitsoq? Graphite in metamorphic rocks can be precipitated from carbonic fluids or melts (Pasteris, 1999; Luque et al., 2014) or due to the metamorphism of organic matter (e.g. Ohtomo et al., 2014; Taner et al., 2017). Carbon in metamorphic fluids can be derived from decarbonation reactions in carbonates or calc-silicate rocks associated with prograde metamorphism (e.g. Valley and Essene, 1980), sourced from igneous

rocks generated by partial melting of metasomatized mantle (e,g, Frezzotti and Touret, 2014), or from the breakdown of organic material and the mobilization of the carbon-bearing fluid (e.g. Zhang and Santosh, 2019).

Graphite derived from organic material is expected to have isotopically light $\delta^{13}C$ signatures of –49 to –18 ‰ (Vienna Pee Dee Belemnite (VPDB); Schidlowski 1987; 2001) whereas carbon from the mantle is expected to have isotopically heavier values between –8 and –3 ‰ (e.g. Javoy et al., 1986) and carbonates have $\delta^{13}C$ values of ~ 0 (Schidlowski, 2001). Measured values of graphitic carbon from sample 464 range from –13 to –17 ‰ (Table 2); these values are lighter than organic material but heavier than mantle or carbonate carbon. Graphite precipitated from carbonaceous fluids will experience fractionation in carbon isotopes as a function of temperature (Bottinga, 1968) and Rayleigh-type fractionation if the fluid is in a closed system (Satish-Kumar et al., 2011). This process can lead to heavier $\delta^{13}C$ values and we now evaluate the possibility that our measured values can be produced from fractionation of an isotopically lighter source, such as carbonates or the mantle.

Single- or multi-stage precipitation of graphite from a carbonaceous fluid will result in progressively lighter $\delta^{13}C$ values as the fraction of fluid decreases (Horita, 2001; Ray, 2009). For metamorphism of carbonaceous matter, graphite in high-temperature metamorphic rocks is isotopically heavier than graphite in similar rocks at low grade (Hoefs and Frey, 1976; Wada et al., 1994). Nonetheless, once graphite is formed, isotopic resetting is unlikely due to the very slow kinetics of isotopic exchange (e.g. Valley and O'Neil, 1981). We first apply a Rayleigh isotope fractionation model for graphite precipitation from CO_2 using an initial $\delta^{13}C$ value of –2.5 ‰, which is an average for carbonates from the neighbouring Isua supracrustal belt (Schidlowski et al., 1979). We apply the single component fractionation model of Ray (2009) using the fractionation factors of Scheele and Hoefs (1992) at temperatures of 500 °C, 600 °C and 700 °C, which brackets the estimated temperature of corundum growth from phase equilibrium modelling (Fig. 9) and is inferred to be representative of the temperatures of metamorphism in the region at this time at similar crustal levels. The modelled isotopic ratio of graphite as a function of the fraction of CO_2 fluid remaining in the system is shown in Fig. 12a. The lowest modelled value achieved for graphite generated from a CO_2-rich fluid is –13.0 ‰, which is predicted for graphite initially precipitated at 500 °C (Fig. 12). All measured isotope compositions of graphite have lighter carbon isotope ratios than the modelled results (Fig. 12) and precipitation of graphite from a fluid derived from a carbonate similar to those in the Isua supracrustal belt is unlikely.

Considering that fluid in equilibrium with the peak metamorphic (and corundum-bearing) assemblage was expected to contain some CH_4 in addition to CO_2 (Fig. 7), we also apply a multi-component mixing model to evaluate if fractionation of a multi-component fluid derived from Isua supracrustal belt carbonates could result in the light isotope values measured in graphite from the corundum-bearing samples. Even considering a large spectrum of CH_4/CO_2 ratios in the initial fluid, the multi-component model does not predict values similar to those measured from graphite in the samples (Fig. 12b). Therefore, fractionation of a carbonaceous fluid derived from carbonate-rich metasedimentary rocks is ruled out as a possible origin for the fluid associated with corundum growth in the Maniitsoq region.

Other than derivation from biogenic material, additional explanations for the isotopically light values of carbon from sample 464 include disproportionation of siderite and the incorporation of meteoritic carbon. Thermal decomposition of siderite was proposed to relate to isotopically light values of graphite in the Isua supracrustal belt (e.g. van Zuilen et al., 2003; Lepland et al., 2005). A product of this reaction is the generation of magnetite, which is abundant in the Isua supracrustal rocks (van Zuilen et al., 2003), but absent from corundum schists (sample 464) in the Maniitsoq region. Therefore, siderite breakdown is not a cause of the isotopically light values of carbon in the corundum schist. Meteoritic carbon as a source of the isotopically light $\delta^{13}C$ values in graphite is ruled out as a potential source as there is no evidence of other components that would reflect meteorite involvement (e.g. enrichments in Ni) in sample 464 (Yakymchuk and Szilas, 2018) and no evidence for a bolide impact in the region (Yakymchuk et al., 2021). Consequently, the most likely source for carbon that now forms graphite in sample 464 is biogenic material from the metasedimentary package that hosts the corundum schist and the aluminosilicate gneiss.

Metamorphism of primary organic material is expected to result in isotopically heavier values in graphite due to preferential loss of isotopically light methane (Morikiyo, 1986; Luque et al., 2012). Although the measured $\delta^{13}C$ values (–13‰) are isotopically heavier than bona fide biological signatures (–16‰; Schidlowski, 2001), the corundum schist has been subjected to amphibolite facies metamorphism and the carbon isotope value of the precursor to the graphite was likely isotopically lighter. Considering this possible shift of a few per mil, the carbon isotope values of the inferred organic material—now represented by graphite in sample 464—are within the range of cyanobacteria (Schidlowski, 2001). On balance, the best explanation for the source of carbon for graphite in the corundum schist from the Maniitsoq region was precursor organic matter; there is minor graphite in the aluminosilicate gneiss (sample 462), which is the inferred precursor to the corundum schist.

An alternative source of carbon is a distal carbon-rich metasedimentary rock undergoing decarbonation reactions. The absence of measured $\delta^{13}C$ values from sample 464 are inconsistent with Rayleigh fractionation of a CO_2 fluid.

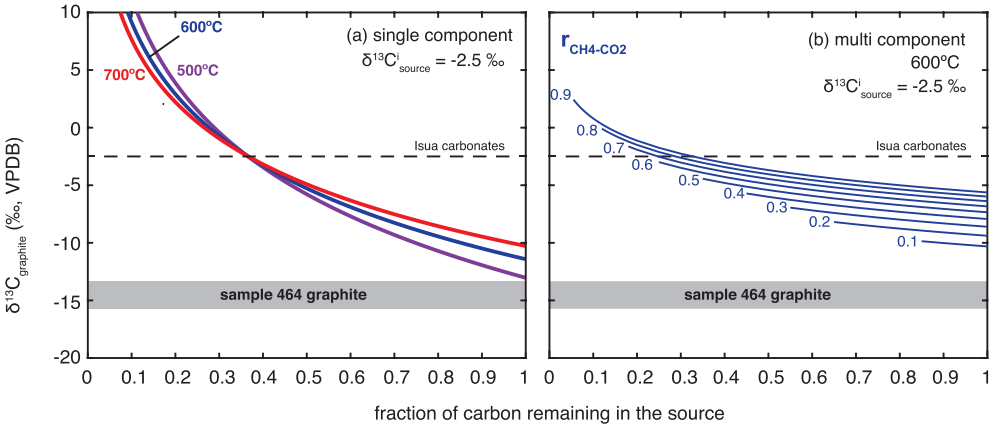

Fig. 12. Isotope fractionation model for the isotopic composition of graphite in equilibrium with CO_2 fluid as a function of the fraction of carbon remaining in the source for: (a) a single component (H_2O–CO_2) system, and (b) a multi-component (H_2O–CO_2–CH_4) system. For the multi-component model, the value $r_{CH4–CO2}$ represents the initial molar ratio of CH_4 to CO_2 in the fluid. The average carbon isotope ratio of carbonates from the neighbouring Isua supracrustal belt (Schidlowski et al., 1979) is used as an approximation for the value of carbonate-rich material that may have been involved in graphite petrogenesis in the Maniitsoq region. The $\delta^{13}C$ values of acid-treated bulk separates (estimated to be close to the value of graphite) from sample 464 are shown by the grey horizontal line. Even for low temperatures (~500 °C), the

macroscopic evidence of fluid–rock interaction at outcrop (i.e. absence of macroscopic carbonate minerals in corundum-bearing rocks) is inconsistent with infiltration of an externally-derived fluid. Furthermore, graphite forms inclusions in corundum in sample 464 (Fig. 2e, 3c), which suggests that the carbon was present in the system prior to peak metamorphism; the simplest explanation is that the carbon was sourced from the sedimentary protolith (e.g. sample 462). Considering the different modes of graphite between the aluminosilicate gneiss (<1 vol %) and the corundum schist (~2 vol%, but locally higher), we acknowledge the possibility that the sedimentary horizon now represented by sample 464 was slightly different than the aluminosilicate gneiss, which was discussed by Yakymchuk and Szilas (2018). The presence of graphite in the metasedimentary precursor to the corundum schist is also consistent with the calculated fluid compositions (Fig. 7) and reduced water activity inferred from phase equilibrium modelling (Fig. 9b). In summary, the presence of biogenic carbon in the protolith of sample 464 created a reduced-a_{H2O} environment that was a prerequisite to generate the amphibolite-facies corundum-bearing assemblage at the Maniitsoq corundum occurrence. Graphite from the Storø ruby occurrence in southern West Greenland also displays $\delta^{13}C$ values consistent with organic material (van Hinsberg et al., 2021).

6.4. Rutile ages

The U–Pb ages retrieved from rutile can provide an absolute age constraint on corundum growth given their spatial (and inferred genetic) association; but, this first requires an assessment of the microstructural setting of rutile coupled with an appraisal of the closure temperature of rutile to radiogenic Pb diffusion. Rutile occurs as inclusions in corundum, plagioclase (Fig. 11a) and along grain boundaries (Fig. 3a, b, c, e); it is predicted to be stable at $T < 630$ °C for the modelled rock composition and an equilibrium assemblage with rutile and corundum is restricted to $T < 600$ °C (Fig. 9). However, the modelled stability of rutile is sensitive to oxidation state of the system (e.g. Diener and Powell, 2010), which may have changed over the *P–T* evolution due to the changes in fluid composition (e.g. Harlov et al., 2006). The oxide mineral assemblage can also vary across a sample due to the local chemical environment (e.g. Bose et al., 2009). Finally, the paucity of ilmenite in corundum-rich domains and measurable concentrations of Fe_2O_3 in corundum (Fig. 5c, d) suggest that corundum was a significant sink for ferric iron, but this is not considered in the phase equilibrium modelling where corundum is treated as pure Al_2O_3. Considering all of these factors, we treat the temperature constraints on rutile stability determined from phase equilibrium modelling with caution as rutile may have been stable at higher temperatures than implied from the modelling. Petrographic observations of rutile also support an inference that rutile was stable during prograde and retrograde portions of the *P–T* evolution of the corundum schist. The presence of rutile inclusions in minerals (e.g. corundum) that are expected to grow during the prograde evolution (Yakymchuk and Szilas, 2018) is compatible with early prograde rutile growth and the presence of interstitial idioblastic rutile is consistent with rutile stability during cooling (Fig. 3a). These observations and estimated temperatures have implications for interpreting the geological significance of the U–Pb rutile ages from the corundum schist.

There are variable estimates for the closure temperature of Pb in rutile and it is sensitive to grain size and shape as well as the cooling history of the terrane (Kooijman et al., 2010; Meinhold, 2010). Nevertheless, the closure temperature for Pb in rutile is generally expected to be ~ 600 °C for a ~ 200 μm grain (Cherniak, 2000) and our estimated temperatures of corundum growth are 600–700 °C; this suggests that rutile in the corundum schist was susceptible to thermally activated loss of radiogenic-Pb through volume (lattice) diffusion. This interpretation is supported by two additional observations. First, the age of a mapped rutile grain generally increases towards the centre of the grain, consistent with greater retention of radiogenic Pb towards the interior (Fig. 11c), that is the core to rim profile reflects (at least in part) a diffusion profile. Second, the data from individual grains and the mapped rutile grain scatter along a single discordia array (which is, for many analyses, within uncertainty of concordia; Fig. 10b). Therefore, our preferred interpretation is that the upper intercept age indicates rutile growth at *c.* 2.5 Ga followed by domainal radiogenic Pb loss associated with amphibolite-facies conditions at this time. Such temperatures could have allowed radiogenic-Pb loss in some rutile domains that were open to faster diffusion pathways. We note that the end of the mapped rutile grain next to plagioclase retains apparently older $^{207}Pb/^{206}Pb$ ages. We interpret this feature to reflect the lack of appropriate sink for Pb within the plagioclase which itself could have been in the process of minor Pb diffusion during a ~ 600–700 °C thermal event (Cherniak, 1995). Nonetheless, one cannot rule out the possibility that there was a sink for Pb in the third dimension, i.e. outside the plane of the analyzed thin section (Fig. 11).

6.5. Regional implications

New U–Pb zircon geochronology from sample 464 indicates a Mesoarchean–Neoarchean detrital component with the youngest inferred detrital zircon yielding an age of 2861 ± 15 Ma (Supplementary Table S3). The youngest single age on an inferred detrital component of zircon is within the depositional range suggested for supracrustal rocks in the Kangerluarssuk supracrustal rocks (2877–2857 Ma; Kirkland et al., 2018a). Analyses of zircon rims or discrete homogenous grains in the corundum schist (sample 464) yield $^{207}Pb/^{206}Pb$ ages that range from *c.* 2722 to 2595 Ma and are interpreted to represent metamorphism (or the effects of metamorphism on protolith material). These ages are generally younger than the timing of metamorphic events that affected the Nuuk region to the south (*c.* 2857–2700 Ma; Nutman and Friend, 2007; Nutman et al., 2007; Szilas et al., 2020) and mostly younger than the inferred age of corundum growth in the Fiskenæsset complex (2.72–2.70 Ga; Keulen et al., 2014). However, these ages are compatible with the minimum age of ruby growth and metasomatism of *c.* 2.50 Ga (rutile U–Pb geochronology) at the Storø ruby locality in the Nuuk terrane assemblage (van Hinsberg et al., 2021). In addition, the *c.* 2.7–2.6 Ga ages related to metamorphism at the Maniitsoq corundum occurrence are also younger than the timing of high-temperature metamorphism that affected the Kangerluarssuk supracrustal rocks at the northern margin of the Akia Terrane (Kirkland et al., 2018a), but they do fall within the range of apatite from an altered tonalite that was inferred to represent amphibolite-facies metamorphism in the late Neoarchean to early Paleoproterozoic (Kirkland et al., 2018b).

Rutile geochronology provides constraints on the approximate age of corundum growth at the Maniitsoq occurrence. The apparent 2503 ± 58 Ma age of rutile from the corundum schist is younger than many of the major tectonometamorphic events across the Akia Terrane. Nonetheless, the age is similar to granitic leucosomes in amphibolite which yield a weighted mean $^{207}Pb/^{206}Pb$ date of 2537 ± 11 Ma (sample 310 from Kirkland et al., 2020), an undeformed *c.* 2.56 Ga granite that cuts regional deformation fabrics (sample 215 from Gardiner et al., 2019), and eight xenocrystic zircons in a kimberlite dyke that yield $^{207}Pb/^{206}Pb$ ages of 2.52–2.42 Ga (Gardiner et al., 2020). These late Neoproterozoic ages are also similar to *c.* 2.56 Ga metamorphic zircon (Dyck et al., 2015) within a high strain zone (Alanngua complex) between the Mesoarchean Akia and Meso- to Neoarchean Tuno terranes (Friend and Nutman, 1994), although these rocks record higher peak metamorphic temperatures (~800 °C; Dyck et al., 2015) than inferred from our samples (~600–700 °C; Figs. 6, 9).

Late Neoarchean magmatic activity of a similar age to that inferred for corundum growth at the Maniitsoq locality is rare in southern West Greenland. The Qôrqut Granite Complex in the Nuuk terrane assemblage (Fig. 1) crystallized at *c.* 2.56 Ga (Friend et al., 1988; Friend and Nutman 2005; Nutman et al., 1989; Crowley 2002). This granite complex may have been associated with the influx of volatiles from the breakdown of hydrous minerals (Brown et al., 1981), the descent of meteoric fluids

(Nutman et al., 2010), or by amphibole breakdown at pressures of 13–18 kbar (Næraa et al., 2014). Regardless, the generation and emplacement of the Qôrqut Granite Complex was associated with a substantial late Neoarchean thermal event in the crust. The Qôrqut Granite Complex is interpreted to have been emplaced in a post-collisional setting (e.g. Næraa et al., 2014) or related to the final stages of arc magmatism (Dyck et al., 2015). Ruby mineralization at Storø in the Nuuk terrane assemblage (Fig. 1) was proposed to be related to fluid released from magmatism associated with the Qôrqut Granite Complex that interacted with metapelites and nearby ultramafic rocks (van Hinsberg et al., 2021). Nevertheless, the late Neoarchean age of the Qôrqut Granite Complex denotes the final stages of cratonization in West Greenland. Although the Qôrqut Granite Complex crops out mostly east to northeast of Nuuk (Fig. 1), xenocrystic zircon in kimberlites from the Maniitsoq region have similar ages and Hf isotope values to the Qôrqut Granite Complex (Gardiner et al., 2020) and suggests that analogous magmatism occurred in the Maniitsoq region in the Akia Terrane.

In addition to late Neoarchean magmatism associated with cratonization in southern West Greenland, further evidence of thermal activity in the Akia Terrane at this time is indicated by *c.* 2.54 Ga titanite that is inferred to be related to a regional fluid influx (Kirkland et al., 2020) and *c.* 2.5 Ga apatite that was proposed to record metamorphic growth at this time (Kirkland et al., 2018b). The age of rutile in our samples from the Maniitsoq corundum locality of *c.* 2.5 Ga is consistent with a late-orogenic regional thermal event that may have locally recorded granulite-facies conditions (Dyck et al., 2015) in the Alanngua complex (Fig. 1). Although the spatial extent of this Late Neoarchean thermal event is not well known outside of the Alanngua complex and from some samples in the northern Akia Terrane, this event appears key in generating the thermochemical conditions for corundum growth during the final stabilization of the Archean North Atlantic Craton at the end of the Archean Eon.

Archean ruby (corundum) deposits are rare (Giuliani et al., 2020). The only economic ruby deposit of Archean age is the Aappaluttoq deposit (Smith et al., 2016), which is thought to have formed at *c.* 2.7 Ga and associated with the pegmatite related fluid–rock alteration in the Fiskenæsset Anorthosite Complex (Fagan, 2018; Keulen et al., 2020). Our results from the Maniitsoq corundum occurrence indicate that a confluence of factors enabled late Archean corundum (ruby) growth, including the presence of aluminous sedimentary rocks with biogenic carbon needed to reduce H_2O activity, the tectonic juxtaposition of ultramafic rocks (source of Cr and needed to reduce silica activity), and late-orogenic magmatism that brought heat and fluids into the system. Although the direct indicators of late-orogenic magmatism (i.e. pegmatites) are not found at all ruby occurrences associated with the Fiskenæsset Anorthosite Complex (Fagan, 2018) or at the Maniitsoq occurrence, substantial late-orogenic Neoarchean heating and fluid flow appear to be a requirement for corundum (ruby) growth in both locations (this study; Keulen et al., 2020) and at the Storø ruby locality (van Hinsberg et al., 2021). The late Archean represents a time of substantial geodynamic change in the Earth (Brown and Johnson, 2018); perhaps the transition into a subduction-dominated geodynamic regime in the Neoarchean enabled more efficient fluid cycling into the deep crust and upper mantle that permitted late-orogenic magmatism and fluid flow that helped drive corundum (ruby) growth. Late-orogenic magmatism and associated fluid flow was also associated with *c.* 2.7–2.6 Ga gold mineralization near Storø region in southern West Greenland (Scherstén et al., 2012; Szilas et al., 2020). The evolution of thermochemical factors associated with the Neoarchean transition into subduction-driven tectonics in southern West Greenland culminated in the final stabilization of the North Atlantic Craton and may have been associated with a prolific episode of both corundum (ruby) and other late-orogenic Archean mineral deposits.

7. Conclusions

Corundum in the Maniitsoq region of southern West Greenland grew at *c.* 2.5 Ga at amphibolite-facies conditions (~600–700 °C at ~ 4–7 kbar) at the end of a regional heating event associated with late-orogenic granite emplacement and fluid flow. Rutile U–Pb systematics imply growth at *c.* 2.5 Ga followed by domain-specific radiogenic Pb loss driven by thermally activated volume diffusion. Phase equilibrium and fluid modelling indicate that corundum grew in the presence of a fluid with reduced water activity that also contained a significant component of CO_2. Graphite found with corundum yields $\delta^{13}C$ values indicative of a biogenic origin for carbon. The timing of corundum growth in the Maniitsoq region was probably associated with late-orogenic magmatism in southern West Greenland. Therefore, the growth of corundum is associated with the final stabilization of the Archean North Atlantic Craton. The late Archean was favorable for ruby mineralization due to metamorphism at amphibolite-facies conditions that followed tectonic juxtaposition of Cr-rich ultramafic rocks with aluminous and carbon-rich metasedimentary rocks; this confluence of geological factors enabled late Neoarchean corundum growth in the Maniitsoq region of southern West Greenland.

Declaration of Competing Interest

The authors declare that they have no known competing financial interests or personal relationships that could have appeared to influence the work reported in this paper.

Acknowledgements

The Ministry of Mineral Resources, Greenland Government supported field and analytical work. CY acknowledges support from a National Sciences and Engineering Research Council of Canada Discovery Grant. We thank anonymous reviewers and F.L. Sutherland for constructive comments on this manuscript, and F. Pirajno for editorial handling.

Appendix A. Supplementary data

Supplementary data to this article can be found online at https://doi.org/10.1016/j.oregeorev.2021.104417.

References

Albee, A.L., 1972. Metamorphism of Pelitic Schists - Reaction Relations of Chloritoid and Staurolite. Geol. Soc. Am. Bull. 83, 3249–3268.
Allaart, J.H., 1982. Geologisk kort over Grønland, 1:500 000, Sheet 2 Frederikshåb Isblink - Søndre Strømfjord.
Bose, S., Das, K., Ohnishi, I., Torimoto, J., Karmakar, S., Shinoda, K., Dasgupta, S., 2009. Characterization of oxide assemblages of a suite of granulites from Eastern Ghats Belt, India: Implication to the evolution of C-O–H–F fluids during retrogression. Lithos 113, 483–497.
Bottinga, Y., 1968. Calculation of fractionation factors for carbon and oxygen isotopic exchange in the system calcite-carbon dioxide-water. J. Phys. Chem. 72, 800–808.
Brown, M., Friend, C.R.L., McGregor, V.R., Perkins, W.T., 1981. The Late Archaean Qôrqut Granite Complex of southern west Greenland. J. Geophys. Res. Solid Earth 86, 10617–10632.
Brown, M., Johnson, T., 2018. Secular change in metamorphism and the onset of global plate tectonics. Am. Mineral. 103, 181–196.
Cartwright, I., Barnicoat, A.C., 1986. The generation of quartz-normative melts and corundum-bearing restites by crustal anatexis: petrogenetic modelling based on an example from the Lewisian of North-West Scotland. J. Metamorph. Geol. 4, 79–99.
Cherniak, D.J., 1995. Diffusion of Lead in Plagioclase and K-Feldspar - an Investigation using Rutherford Backscattering and Resonant Nuclear-Reaction Analysis. Contrib. Miner. Petrol. 120, 358–371.
Cherniak, D.J., 2000. Pb diffusion in rutile. Contrib. Miner. Petrol. 139, 198–207.
Chu, X., Ague, J.J., 2013. Phase equilibria for graphitic metapelite including solution of CO2 in melt and cordierite: implications for dehydration, partial melting and graphite precipitation. J. Metamorph. Geol. 31, 843–862.
Connolly, J.A.D., 2005. Computation of phase equilibria by linear programming: A tool for geodynamic modeling and its application to subduction zone decarbonation. Earth Planet. Sci. Lett. 236, 524–541.

Crowley, J.L., 2002. Testing the model of late Archean terrane accretion in southern West Greenland: a comparison of the timing of geological events across the Qarliit nunaat fault, Buksefjorden region. Precambr. Res. 116, 57–79.
de Capitani, C., Brown, T.H., 1987. The computation of chemical equilibrium in complex systems containing non-ideal solutions. Geochim. Cosmochim. Acta 51, 2639–2652.
de Capitani, C., Petrakakis, K., 2010. The computation of equilibrium assemblage diagrams with Theriak/Domino software. Am. Mineral. 95, 1006–1016.
de Santis, R., Breedveld, G.J.F., Prausnitz, J.M., 1974. Thermodynamic Properties of Aqueous Gas Mixtures at Advanced Pressures. Ind. Eng. Chem. Process Des. Dev. 13, 374–377.
Deer, W.A., Howie, R.A., Zussman, J., 1992. An Introduction to the Rock-Forming Minerals, second ed. Wiley, New York.
Diener, J.F.A., Powell, R., 2010. Influence of ferric iron on the stability of mineral assemblages. J. Metamorph. Geol. 28, 599–613.
Droop, G., 1987. A General Equation for Estimating Fe-3+ Concentrations in Ferromagnesian Silicates and Oxides from Microprobe Analyses, using Stoichiometric Criteria. Mineral. Mag. 51, 431–435.
Dyck, B., Reno, B.L., Kokfelt, T.F., 2015. The Majorqaq Belt: A record of Neoarchaean orogenesis during final assembly of the North Atlantic Craton, southern West Greenland. Lithos 220, 253–271.
Ewing, T.A., 2011. Hf isotope analysis and U-Pb geochronology of rutile : technique development and application to a lower crustal section (Ivrea-Verbano Zone, Italy). PhD Dissertation. Australian National University, p. 385.
Fagan, A.J., 2018. The ruby and pink sapphire deposits of SW Greenland: geological setting, genesis, and exploration techniques. PhD Dissertation. University of British Columbia, p. 747.
Frezzotti, M., Touret, J.L.R., 2014. CO2, carbonate-rich melts, and brines in the mantle. Geosci. Front. 5, 697–710.
Friend, C.R.L., Nutman, A.P., 2019. Tectono-stratigraphic terranes in Archaean gneiss complexes as evidence for plate tectonics: The Nuuk region, southern West Greenland. Gondwana Res. 72, 213–237.
Friend, C., Nutman, A.P., 1994. Archean Granulite-Facies Metamorphic Events in the Nuuk-Maniitsoq Region, Southern West Greenland - Correlation with the Saglek Block, Labrador. J. Geol. Soc. 151, 421–424.
Friend, C., Nutman, A.P., 2001. U-Pb zircon study of tectonically bounded blocks of 2940–2840 Ma crust with different metamorphic histories, Paamiut region, South-West Greenland: implications for the tectonic assembly of the North Atlantic craton. Precambr. Res. 105, 143–164.
Friend, C., Nutman, A.P., 2005. Complex 3670–3500 Ma orogenic episodes superimposed on juvenile crust accreted between 3850 and 3690 Ma, Itsaq Gneiss Complex, Southern West Greenland. J. Geol. 113, 375–397.
Friend, C., Nutman, A.P., McGregor, V.R., 1988. Late Archean Terrane Accretion in the Godthab Region, Southern West Greenland. Nature 335, 535–538.
Frost, B.R., Chacko, T., 1989. The Granulite Uncertainty Principle - Limitations on Thermobarometry in Granulites. J. Geol. 97, 435–450.
Garde, A.A., Marker, M., 1988. Corundum crystals with blue-red color zoning near Kangerdluarssuk, Sukkertoppen district, West Greenland. Bull. Geol. Soc. Den. 140, 46–49.
Gardiner, N.J., Kirkland, C.L., Hollis, J., Szilas, K., Steenfelt, A., Yakymchuk, C., Heide-Jorgensen, H., 2019. Building Mesoarchaean crust upon Eoarchaean roots: the Akia Terrane, West Greenland. Contrib. Miner. Petrol. 174, 20.
Gardiner, N.J., Kirkland, C.L., Hollis, J.A., Cawood, P.A., Nebel, O., Szilas, K., Yakymchuk, C., 2020. North Atlantic Craton architecture revealed by kimberlite-hosted crustal zircons. Earth Planet. Sci. Lett. 534, 116091.
Giuliani, G., Dubessy, J., Banks, D., Hoàng Quang, V., Lhomme, T., Pironon, J., Garnier, V., Phan Trong, T., Pham Van, L., Ohnenstetter, D., Schwarz, D., 2003. CO2–H2S–COS–S8–AlO(OH)-bearing fluid inclusions in ruby from marble-hosted deposits in Luc Yen area, North Vietnam. Chem. Geol. 194, 167–185.
Giuliani, G., Groat, L.A., Fallick, A.E., Pignatelli, I., Pardieu, V., 2020. Ruby Deposits: A Review and Geological Classification. Minerals 10.
Harlov, D., Tropper, P., Seifert, W., Nijland, T., Förster, H., 2006. Formation of Al-rich titanite (CaTiSiO4O–CaAlSiO4OH) reaction rims on ilmenite in metamorphic rocks as a function of fH2O and fO2. Lithos 88, 72–84.
Hawthorne, F.C., Oberti, R., Harlow, G.E., Maresch, W.V., Martin, R.F., Schumacher, J. C., Welch, M.D., 2012. Nomenclature of the amphibole supergroup. Am. Mineral. 97, 2031–2048.
Henry, D.J., Guidotti, C.V., Thomson, J.A., 2005. The Ti-saturation surface for low-to-medium pressure metapelitic biotites: Implications for geothermometry and Ti-substitution mechanisms. Am. Mineral. 90, 316–328.
Herd, R.K., Windley, B.F., Ghisler, M., 1969. The mode of occurrence and petrogenisesis of the sapphirine-bearing and associated rocks of West Greenland. Rapp. Grønlands Geol. Unders. 24, 1–44.
Hoefs, J., Frey, M., 1976. The isotopic composition of carbonaceous matter in a metamorphic profile from the Swiss Alps. Geochim. Cosmochim. Acta 40, 945–951.
van Hinsberg, V., Yakymchuk, C., Jepsen, A., Kirkland, C.L., Szilas, K., 2021. The corundum conundrum: Constraining the compositions of meta-somatising fluids involved in corundum formation in high-grade metamorphic melanges of ultramafic and aluminous lithologies. Chem. Geol. 571, 120180.
van Hinsberg, V.J., Schumacher, J.C., 2007. Using estimated thermodynamic properties to model accessory phases: the case of tourmaline. J. Metamorph. Geol. 25, 769–779.
Holland, T.J.B., Powell, R., 2011. An improved and extended internally consistent thermodynamic dataset for phases of petrological interest, involving a new equation of state for solids. J. Metamorph. Geol. 29, 333–383.
Holland, T., Powell, R., 2003. Activity-composition relations for phases in petrological calculations: an asymmetric multicomponent formulation. Contrib. Miner. Petrol. 145, 492–501.
Horita, J., 2001. Carbon isotope exchange in the system CO2-CH4 at elevated temperatures. Geochim. Cosmochim. Acta 65, 1907–1919.
Jackson, S.E., Pearson, N.J., Griffin, W.L., Belousova, E.A., 2004. The application of laser ablation-inductively coupled plasma-mass spectrometry to in situ U-Pb zircon geochronology. Chem. Geol. 211, 47–69.
Jacobs, G.K., Kerrick, D.M., 1981. Methane - an Equation of State with Application to the Ternary-System H2o-Co2-Ch4. Geochim. Cosmochim. Acta 45, 607–614.
Javoy, M., Pineau, F., Delorme, H., 1986. Carbon and Nitrogen Isotopes in the Mantle. Chem. Geol. 57, 41–62.
Kalsbeek, F., Taylor, P.N., 1985. Age and Origin of Early Proterozoic Dolerite Dykes in Southwest Greenland. Contrib. Miner. Petrol. 89, 307–316.
Keulen, N., Kalvig, P., 2013. Fingerprinting of corundum (ruby) from Fiskenæsset, West Greenland. GEUS Bulletin 28, 53–56.
Keulen, N., Schumacher, J.C., Naeraa, T., Kokfelt, T.F., Schersten, A., Szilas, K., van Hinsberg, V.J., Schlatter, D.M., Windley, B.F., 2014. Meso- and Neoarchaean geological history of the Bjornesund and Ravns Storo Supracrustal Belts, southern West Greenland: Settings for gold enrichment and corundum formation. Precambr. Res. 254, 36–58.
Keulen, N., Thomsen, T.B., Schumacher, J.C., Poulsen, M.D., Kalvig, P., Vennemann, T., Salimi, R., 2020. Formation, origin and geographic typing of corundum (ruby and pink sapphire) from the Fiskenæsset complex. Greenland. Lithos 105536.
Kirkland, C.L., Yakymchuk, C., Gardiner, N.J., Szilas, K., Hollis, J., Olierook, H., Steenfelt, A., 2020. Titanite petrochronology linked to phase equilibrium modelling constrains tectono-thermal events in the Akia Terrane, West Greenland. Chem. Geol. 536, 119467.
Kirkland, C.L., Yalcymchuk, C., Hollis, J., Heide-Jorgensen, H., Danigik, M., 2018a. Mesoarchean exhumation of the Akia terrane and a common Neoarchean tectonothermal history for West Greenland. Precambr. Res. 314, 129–144.
Kirkland, C.L., Yakymchuk, C., Szilas, K., Evans, N., Hollis, J., McDonald, B., Gardiner, N. J., 2018b. Apatite: a U-Pb thermochronometer or geochronometer? Lithos 318, 143–157.
Kooijman, E., Mezger, K., Berndt, J., 2010. Constraints on the U-Pb systematics of metamorphic rutile from in situ LA-ICP-MS analysis. Earth Planet. Sci. Lett. 293, 321–330.
Krebs, M.Y., Pearson, D.G., Fagan, A.J., Bussweiler, Y., Sarkar, C., 2019. The application of trace elements and Sr–Pb isotopes to dating and tracing ruby formation: The Aappaluttoq deposit, SW Greenland. Chem. Geol. 523, 42–58.
Lepland, A., van Zuilen, M.A., Arrhenius, G., Whitehouse, M.J., Fedo, C.M., 2005. Questioning the evidence for Earth's earliest life - Akilia revisited. Geology 33, 77–79.
Li, X.H., Long, W.G., Li, Q.L., Liu, Y., Zheng, Y.F., Yang, Y.H., Chamberlain, K.R., Wan, D. F., Guo, C.H., Wang, X.C., Tao, H., 2010. Penglai zircon megacrysts: a potential new working reference material for microbeam determination of Hf–O isotopes and U-Pb age. Geostand. Geoanal. Res. 34, 117–134.
Ludwig, K.R., 2012. User's Manual for Isoplot Version 3.75–4.15: A Geochronological Toolkit for Microsoft Excel, 5. Special Publication, Berkley Geochronological Centre.
Luque, F.J., Crespo-Feo, E., Barrenechea, J.F., Ortega, L., 2012. Carbon isotopes of graphite: Implications on fluid history. Geosci. Front. 3, 197–207.
Luque, F.J., Huizenga, J., Crespo-Feo, E., Wada, H., Ortega, L., Barrenechea, J.F., 2014. Vein graphite deposits: geological settings, origin, and economic significance. Miner. Deposita 49, 261–277.
Luvizotto, G.L., Zack, T., Meyer, H.P., Ludwig, T., Triebold, S., Kronz, A., Muenker, C., Stockli, D.F., Prowatke, S., Klemme, S., Jacob, D.E., von Eynatten, H., 2009. Rutile crystals as potential trace element and isotope mineral standards for microanalysis. Chem. Geol. 261, 346–369.
Marsh, J.H., Jørgensen, T., Petrus, J.A., Hamilton, M.A., Mole, D.R., 2019. U-Pb, trace element, and hafnium isotope composition of the Maniitsoq zircon: a potential new Archean zircon reference material. Goldschmidt Abstract 2161.
McLellan, E., 1985. Staurolite Breakdown and the Formation of Kyanite and Sillimanite in the Barrovian Type Area. Journal of the Geological Society 142, 5.
Meinhold, G., 2010. Rutile and its applications in earth sciences. Earth Sci. Rev. 102, 1–28.
Morikiyo, T., 1986. Hydrogen and Carbon Isotope Studies on the Graphite-Bearing Metapelites in the Northern Kiso District of Central Japan. Contrib. Miner. Petrol. 94, 165–177.
Nutman, A.P., Friend, C., Baadsgaard, H., McGregor, V.R., 1989. Evolution and Assembly of Archean Gneiss Terranes in the Godthabsfjord Region, Southern West Greenland - Structural, Metamorphic, and Isotopic Evidence. Tectonics 8, 573–589.
Næraa, T., Kemp, A.I.S., Schersten, A., Rehnstrom, E.F., Rosing, M.T., Whitehouse, K.J., 2014. A lower crustal mafic source for the ca. 2550 Ma Qorqut Granite Complex in southern West Greenland. Lithos 192, 291–304.
Nutman, A.P., Christiansen, O., Friend, C.R.L., 2007. 2635 Ma amphibolite facies gold mineralisation near a terrane boundary (suture?) on Storo, Nuuk region, southern West Greenland. Precambr. Res. 159, 19–32.
Nutman, A.P., Friend, C.R.L., 2007. Adjacent terranes with ca. 2715 and 2650 Ma high-pressure metamorphic assemblages in the Nuuk region of the North Atlantic Craton, southern West Greenland: Complexities of Neoarchaean collisional orogeny. Precambr. Res. 155, 159–203.
Nutman, A.P., Friend, C.R.L., Hiess, J., 2010. Setting of the 2560 Ma Qorqut Granite Complex in the Archean crustal evolution of southern West Greenland. Am. J. Sci. 310, 1081–1114.
Ohmoto, H., Kerrick, D., 1977. Devolatilization Equilibria in Graphitic Systems. Am. J. Sci. 277, 1013–1044.
Ohtomo, Y., Kakegawa, T., Ishida, A., Nagase, T., Rosing, M.T., 2014. Evidence for biogenic graphite in early Archaean Isua metasedimentary rocks. Nat. Geosci. 7, 25–28.

Owens, B.E., Belkin, H.E., Zerolis, J.M., 2013. Margarite, corundum, gahnite and zincohogbomite in a blackwall, Raleigh Terrane, Eastern Piedmont Province, USA. Mineral. Mag. 77, 2913–2929.
Pasteris, J.D., 1999. Causes of the uniformly high crystallinity of graphite in large epigenetic deposits. J. Metamorph. Geol. 17, 779–787.
Paton, C., Hellstrom, J., Paul, B., Woodhead, J., Hergt, J., 2011. Iolite: Freeware for the visualisation and processing of mass spectrometric data. J. Anal. At. Spectrom. 26, 2508–2518.
Pitzer, K.S., Sterner, S.M., 1994. Equations of State Valid Continuously from Zero to Extreme Pressures for H_2O and CO_2. J. Chem. Phys. 101, 3111–3116.
Polat, A., Appel, P.W.U., Fryer, B.J., 2011. An overview of the geochemistry of Eoarchean to Mesoarchean ultramafic to mafic volcanic rocks, SW Greenland: Implications for mantle depletion and petrogenetic processes at subduction zones in the early Earth. Gondwana Res. 20, 255–283.
Polat, A., Frei, R., Schersten, A., Appel, P.W.U., 2010. New age (ca. 2970 Ma), mantle source composition and geodynamic constraints on the Archean Fiskenaesset anorthosite complex. SW Greenland. Chemical Geology 277, 1–20.
Powell, R., Evans, K.A., Green, E.C.R., White, R.W., 2019. The truth and beauty of chemical potentials. J. Metamorph. Geol. 37, 1007–1019.
Powell, R., Holland, T.J.B., 2008. On thermobarometry. J. Metamorph. Geol. 26, 155–179.
Ramberg, H., 1948. On sapphirine-bearing rocks in the vicinity of Sukkertoppen (West Greenland). Medd. Grønland 142, 31.
Ray, J.S., 2009. Carbon isotopic variations in fluid-deposited graphite: evidence for multicomponent Rayleigh isotopic fractionation. Int. Geol. Rev. 51, 45–57.
Riesco, M., Stuwe, K., Reche, J., 2005. Formation of corundum in metapelites around ultramafic bodies. An example from the Saualpe region, Eastern Alps. Mineral. Petrol. 83, 1–25.
Satish-Kumar, M., Yurimoto, H., Itoh, S., Cesare, B., 2011. Carbon isotope anatomy of a single graphite crystal in a metapelitic migmatite revealed by high-spatial resolution SIMS analysis. Contrib. Miner. Petrol. 162, 821–834.
Scheele, N., Hoefs, J., 1992. Carbon Isotope Fractionation between Calcite, Graphite and Co2 - an Experimental-Study. Contrib. Miner. Petrol. 112, 35–45.
Scherstén, A., Szilas, K., Creaser, R.A., Næraa, T., van Gool, J.A.M., Østergaard, C., 2012. Re–Os and U-Pb constraints on gold mineralisation events in the Meso- to Neoarchaean Storø greenstone belt, Storø, southern West Greenland. Precambr. Res. 200–203, 149–162.
Schidlowski, M., 1987. Application of Stable Carbon Isotopes to Early Biochemical Evolution on Earth. Annu. Rev. Earth Planet. Sci. 15, 47–72.
Schidlowski, M., 2001. Carbon isotopes as biogeochemical recorders of life over 3.8 Ga of Earth history: evolution of a concept. Precambr. Res. 106, 117–134.
Schidlowski, M., Appel, P., Eichmann, R., Junge, C.E., 1979. Carbon Isotope Geochemistry of the 3.7 X 109-Yr-Old Isua Sediments, West Greenland - Implications for the Archaean Carbon and Oxygen Cycles. Geochim. Cosmochim. Acta 43, 189–199.
Simonet, C., Fritsch, E., Lasnier, B., 2008. A classification of gem corundum deposits aimed towards gem exploration. Ore Geol. Rev. 34, 127–133.
Sláma, J., Košler, J., Condon, D.J., Crowley, J.L., Gerdes, A., Hanchar, J.M., Horstwood, M.S.A., Morris, G.A., Nasdala, L., Norberg, N., Schaltegger, U., Schoene, B., Tubrett, M.N., Whitehouse, M.J., 2008. Plešovice zircon—a new natural reference material for U–Pb and Hf isotopic microanalysis. Chem. Geol. 249 (1-2), 1–35.
Smith, C.P., Fagan, A.J., Clark, B., 2016. Ruby and Pink Sapphire from Aappaluttoq, Greenland. J. Gemmol. 35, 294–306.
Spear, F.S., Florence, F.P., 1992. Thermobarometry in Granulites - Pitfalls and New Approaches. Precambr. Res. 55, 209–241.
Stacey, J.S., Kramers, J.D., 1975. Approximation of terrestrial lead isotope evolution by a two-stage model. Earth Planet. Sci. Lett. 26, 207–221.
Steenfelt, A., Hollis, J., Kirkland, C.L., Sandrin, A., Gardiner, N.J., K. H. Olierook, H., Szilas, K., Waterton, P., Yakymchuk, C., 2021. The Mesoarchaean Akia terrane, West Greenland, revisited: New insights based on spatial integration of geophysics, field observation, geochemistry and geochronology. Precambr. Res. 352, 105958.
Stern, R.A., Bodorkos, S., Kamo, S.L., Hickman, A.H., Corfu, F., 2009. Measurement of SIMS Instrumental Mass Fractionation of Pb Isotopes During Zircon Dating. Geostand. Geoanal. Res. 33, 145–168.
Stern, R.J., Tsujimori, T., Harlow, G., Groat, L.A., 2013. Plate tectonic gemstones. Geology 41, 723–726.
Stüwe, K., 1997. Effective bulk composition changes due to cooling: a model predicting complexities in retrograde reaction textures. Contrib. Miner. Petrol. 129, 43–52.
Szilas, K., 2018. A Geochemical Overview of Mid-Archaean Metavolcanic Rocks from Southwest Greenland. Geosciences 8.
Szilas, K., Kelemen, P.B., Bernstein, S., 2015. Peridotite enclaves hosted by Mesoarchaean TTG-suite orthogneisses in the Fiskefjord region of southern West Greenland. GeoResJ 7, 22–34.
Szilas, K., Tusch, J., Herwartz, D., Fonseca, R.O.C., 2020. Two metamorphic gold mineralization events confirmed by Lu-Hf isotope dating of garnet in the Late Archean Storø Au deposit, Nuuk region of SW Greenland. Ore Geol. Rev. 121, 103476.
Szilas, K., van Hinsberg, V., McDonald, I., Naeraa, T., Rollinson, H., Adetunji, J., Bird, D., 2018. Highly refractory Archaean peridotite cumulates: Petrology and geochemistry of the Seqi Ultramafic Complex, SW Greenland. Geosci. Front. 9, 689–714.
Taner, M.F., Drever, C., Yakymchuk, C., Longstaffe, F.J., 2017. Origin of Graphite in the Southwestern Grenville Province. Can. Mineral. 55, 1041–1055.
Valley, J.W., Essene, E.J., 1980. Calc-silicate reactions in Adirondack marbles: The role of fluids and solid solutions: Summary. Geol. Soc. Am. Bull. 91, 114–117.
Valley, J.W., O'Neil, J.R., 1981. C-13-C-12 Exchange between Calcite and Graphite - a Possible Thermometer in Grenville Marbles. Geochim. Cosmochim. Acta 45, 411–419.
Wada, H., Tomita, T., Matsuura, K., Iuchi, K., Ito, M., Morikiyo, T., 1994. Graphitization of Carbonaceous Matter during Metamorphism with References to Carbonate and Pelitic Rocks of Contact and Regional Metamorphisms, Japan. Contrib. Miner. Petrol. 118, 217–228.
Waterton, P., Hyde, W.R., Tusch, J., Hollis, J.A., Kirkland, C.L., Kinney, C., Yakymchuk, C., Gardiner, N.J., Zakharov, D., Olierook, H.K.H., Lightfoot, P.C., Szilas, K., 2020. Geodynamic Implications of Synchronous Norite and TTG Formation in the 3 Ga Maniitsoq Norite Belt, West Greenland. Frontiers Earth Sci. 8, 562062. https://doi.org/10.3389/feart.2020.562062.
White, R.W., Powell, R., Clarke, G.L., 2002. The interpretation of reaction textures in Fe-rich metapelitic granulites of the Musgrave Block, central Australia: constraints from mineral equilibria calculations in the system K2O-FeO-MgO-Al2O3-SiO2-H2O-TiO2-Fe2O3. J. Metamorph. Geol. 20, 41–55.
White, R.W., Powell, R., Holland, T., Worley, B.A., 2000. The effect of TiO2 and Fe2O3 on metapelitic assemblages at greenschist and amphibolite facies conditions: mineral equilibria calculations in the system K2O-FeO-MgO-Al2O3-SiO2-H2O-TiO2-Fe2O3. J. Metamorph. Geol. 18, 497–511.
White, R.W., Powell, R., Holland, T.J.B., Johnson, T.E., Green, E.C.R., 2014a. New mineral activity-composition relations for thermodynamic calculations in metapelitic systems. J. Metamorph. Geol. 32, 261–286.
White, R.W., Powell, R., Johnson, T.E., 2014b. The effect of Mn on mineral stability in metapelites revisited: new a-x relations for manganese-bearing minerals. J. Metamorph. Geol. 32, 809–828.
Wiedenbeck, M., Alle, P., Corfu, F., Griffin, W.L., Meier, M., Oberli, F., Vonquadt, A., Roddick, J.C., Speigel, W., 1995. 3 Natural Zircon Standards for U-Th-Pb, Lu-Hf, Trace-Element and Ree Analyses. Geostand. Newslett. 19, 1–23.
Yakymchuk, C., Kirkland, C.L., Cavosie, A.J., Szilas, K., Hollis, J., Gardiner, N.J., Waterton, P., Steenfelt, A., Martin, L., 2021. Stirred not shaken; critical evaluation of a proposed Archean meteorite impact in West Greenland. Earth and Planetary Science Letters 557, 116730. https://doi.org/10.1016/j.epsl.2020.116730.
Yakymchuk, C., Kirkland, C.L., Hollis, J.A., Kendrick, J., Gardiner, N.J., Szilas, K., 2020. Mesoarchean partial melting of mafic crust and tonalite production during high-T low-P stagnant tectonism, Akia Terrane, West Greenland. Precambr. Res. 339, 105615.
Yakymchuk, C., Szilas, K., 2018. Corundum formation by metasomatic reactions in Archean metapelite, SW Greenland: Exploration vectors for ruby deposits within high-grade greenstone belts. Geosci. Front. 9, 727–749.
van Zuilen, M.A., Lepland, A., Teranes, J., Finarelli, J., Wahlen, M., Arrhenius, G., 2003. Graphite and carbonates in the 3.8 Ga old Isua Supracrustal Belt, southern West Greenland. Precambr. Res. 126, 331–348.
Zhang, C., Santosh, M., 2019. Coupled laser Raman spectroscopy and carbon stable isotopes of graphite from the khondalite belt of Kerala, southern India. Lithos 334, 245–253.
Zhang, Z., Ding, H., Dong, X., Tian, Z., Mu, H., Li, M., Qin, S., Niu, Z., Zhang, N., 2018. The Eocene corundum-bearing rocks in the Gangdese arc, south Tibet: Implications for tectonic evolution of the Himalayan orogen. Geosci. Front. 9, 1337–1354.